Active membrane conductances and morphology of a collision detection neuron broaden its impedance profile and improve discrimination of input synchrony

Richard B. Dewell[1] and Fabrizio Gabbiani[1,2]
[1]Department of Neuroscience, Baylor College of Medicine, Houston, TX, USA; [2]Department of Electrical and Computer Engineering, Rice University, Houston, TX, USA

Running head: Impedance profile of a collision detection neuron

Corresponding authors:
Fabrizio Gabbiani - gabbiani@bcm.edu
Richard B. Dewell - dewell@bcm.edu

Abstract

Brains processes information through the coordinated efforts of billions of individual neurons, each encoding a small part of the overall information stream. Central to this is how neurons integrate and transform complex patterns of synaptic inputs. The neuronal membrane impedance sets the gain and timing for synaptic integration, determining a neuron's ability to discriminate between synaptic input patterns. Using single and dual dendritic recordings *in vivo*, pharmacology, and computational modeling, we characterized the membrane impedance of a collision detection neuron in the grasshopper, *Schistocerca americana*. We examined how the cellular properties of the lobula giant movement detector (LGMD) neuron are tuned to enable the discrimination of synaptic input patterns key to its role in collision detection. We found that two common active conductances g_H and g_M, mediated respectively by hyperpolarization-activated cyclic nucleotide gated (HCN) channels and by muscarine sensitive M-type K^+ channels, promote broadband integration with high temporal precision over the LGMD's natural range of membrane potentials and synaptic input frequencies. Additionally, we found that the LGMD's branching morphology increased the gain and decreased delays associated with the mapping of synaptic input currents to membrane potential. We investigated whether other branching dendritic morphologies fulfill a similar function and found this to be true for a wide range of

morphologies, including those of neocortical pyramidal neurons and cerebellar Purkinje cells. These findings further our understanding of the integration properties of individual neurons by showing the unexpected role played by two widespread active conductances and by dendritic morphology in shaping synaptic integration.

New & Noteworthy

Neuronal integration depends on complex interactions between synaptic input patterns and the electrochemical properties of dendrites. We used an identified collision detection neuron in grasshoppers to examine how its morphology and two membrane conductances determine the gain and timing of synaptic integration in relation to the computations it performs. The neuronal properties examined are ubiquitous and therefore further a general understanding of neuronal computations, including those in our own brain.

Keywords: dendritic processing, collision avoidance, impedance, lobula giant movement detector

Introduction

By the nineteen forties, neuroscientists had recognized that neuronal membranes exhibited a frequency dependent impedance and had begun investigating which cellular mechanisms contributed to their resistance, capacitance, and inductance (Cole 1941). The capacitance of the membrane is determined by its lipid bilayer, and its resistance by permeability to ion fluxes, but the inductance came from an unknown source. After the discovery of active conductances, it became clear that their kinetics produced a phenomenological inductance, and that its properties could be investigated using Hodgkin and Huxley's equations (Mauro 1961; Mauro et al. 1970).

Membrane capacitance low-passes, while inductance high-passes input currents. Their combination can thus result in bandpass filtering and resonance. In the decades since, researchers have learned a great deal about the roles of active conductances in shaping the electrical properties of

53 neurons, and the influence of neuronal bandpass properties on rhythmic activity within neural networks
54 (Das et al. 2017; Hutcheon and Yarom 2000; Wang 2010). In addition to generating neural rhythms, the
55 membrane impedance shapes the integration properties of dendrites determining their ability to
56 discriminate between patterns of synaptic inputs.

57 Voltage-gated channels modify the membrane impedance through their time varying
58 conductances. The range of input frequencies affected depends on the channel kinetics. Non-
59 inactivating channels that decrease their conductance as the membrane potential approaches their
60 reversal potential produce negative feedback on changes in membrane potential and thus a
61 phenomenological inductance. In the LGMD two such inductive channels, HCN and M, produce the
62 largest resting conductances, influencing the selectivity and timing of its responses (Dewell and
63 Gabbiani 2018a, 2018b). The impedance profile of a neuron is also influenced by its dendritic
64 morphology. An extended morphology causes dendritic compartmentalization which increases the
65 attenuation and lag of postsynaptic potentials traveling towards the spike initiation zone, but
66 simultaneously enhances local coincidence detection and nonlinear processing (Häusser and Mel 2003;
67 London and Hausser 2005). Dendritic branching and tapering could optimize synaptic integration by
68 increasing the spatial homogeneity of postsynaptic potentials' influence at the site of spike initiation
69 (Cuntz et al. 2007). Additionally, the dendritic morphology of pyramidal and Purkinje neurons is
70 believed to favor the neurons' response to inputs of certain frequencies thus promoting neuronal
71 resonance (Dhupia et al. 2015; Ostojic et al. 2015).

72 We have chosen to explore these questions in the LGMD (O'Shea and Williams 1974), an
73 identified neuron in locusts that selectively responds to visual stimuli mimicking impending collision
74 (Rind and Simmons 1992; Schlotterer 1977). The LGMD's stimulus selectivity arises from the precise
75 spatiotemporal patterning of synaptic inputs (Jones and Gabbiani 2010; Peron et al. 2007a; Zhu and
76 Gabbiani 2016) and complex dendritic computations, including filtering by active conductances such
77 as sodium, low voltage calcium, calcium-dependent potassium, inactivating potassium, HCN, and M

78 channels (Dewell and Gabbiani 2018a, 2018b; Gabbiani et al. 2002; Peron and Gabbiani 2009).
79 Different aspects of the LGMD's firing patterns – including burst firing – have been tied to the
80 generation of escape behaviors (Dewell and Gabbiani 2018a; Fotowat et al. 2011; McMillan and Gray
81 2015). Currently, no one has characterized the LGMD's membrane impedance to determine how it
82 shapes this neuron's dendritic integration and visual computations.

83 Neuronal membrane properties have mainly been studied with cultured neurons or brain slices
84 and the natural synaptic input patterns are still unknown for most neurons, so much remains
85 unanswered about how the impedance properties of neurons influence synaptic integration and neural
86 computations *in vivo*. As both g_H and g_M are sensitive to numerous modulators (Delmas and Brown
87 2005; Wahl-Schott and Biel 2009), our ability to conduct experiments *in vivo* ensures that the channels
88 are in the relevant modulatory state. We discovered that the LGMD membrane impedance is broadband
89 and generates small delays between synaptic current and membrane potential that remain consistent
90 across membrane potentials. The HCN and M channels, their interactions, and the neuronal
91 morphology all contribute to producing this broadband impedance profile which increases the LGMD's
92 ability to discriminate behaviorally relevant patterns of synaptic inputs from irrelevant ones.

93 Materials and Methods

94 Animals

95 Experiments were performed on adult female grasshoppers 7-12 weeks of age (*Schistocerca*
96 *americana*). Animals were reared in a crowded laboratory colony under 12 h light/dark conditions.
97 Animals were selected for health and size without randomization, and investigators were not blinded to
98 experimental conditions. Sample sizes were not predetermined before experiments. The surgical
99 procedures used have been described previously (Dewell and Gabbiani 2018a; Gabbiani and Krapp
100 2006a; Jones and Gabbiani 2012).

101 Visual stimuli

102 Visual stimuli were generated using Matlab (RRID:SCR_001622) and the Psychophysics
103 Toolbox (PTB-3, RRID:SCR_002881) on a personal computer running Windows XP. A conventional
104 cathode ray tube monitor refreshed at 200 frames per second was used for stimulus display (LG
105 Electronics, Seoul, Korea). Looming stimuli are the two-dimensional projections of an object
106 approaching on a collision course with the animal. They consisted of an expanding dark square
107 simulating a solid object with half size l approaching at constant speed v (illustrated in Figure 1B). The
108 expansion profile is characterized by the ratio $l/|v|$, as previously described (Gabbiani et al. 2001).

109 **Electrophysiology**

110 Sharp-electrode LGMD intracellular recordings were carried out in current-clamp or voltage-
111 clamp mode using thin walled borosilicate glass pipettes (outer/inner diameter: 1.2/0.9 mm; WPI,
112 Sarasota, FL; see Jones and Gabbiani, 2012, as well as Dewell and Gabbiani, 2018a for details). The
113 membrane potential (V_m) and current (I_m) were low-pass filtered with cutoff frequencies of 10 kHz and
114 5 kHz, respectively. Most recordings were digitized at a sampling rate of 20,073 Hz (for some
115 experiments V_m was digitized at 40,146 Hz). We used a single electrode clamp amplifier capable of
116 operating in discontinuous mode at high switching frequencies (20-35 kHz; SEC-10, NPI, Tamm,
117 Germany). Responses to current injections were recorded in discontinuous current clamp mode (DCC).
118 For dual recordings we inserted under visual guidance a second sharp electrode into the excitatory
119 dendritic field of the LGMD (see Figure 3A) with a motorized micromanipulator (Sutter Instruments,
120 Novato, CA). Membrane potential was recorded with a second SEC-10 amplifier in bridge mode with
121 electrode resistance and capacitance compensation when not injecting current and in DCC mode while
122 injecting current. Switching frequencies, signal filtering and digitization were identical for both
123 recordings.

124 The physical distance along the dendrites and an estimate of the electrotonic distance between
125 recording electrode pairs were measured as follows. First, all cells were stained with Alexa Fluor 594
126 and imaged with a CCD camera to record electrode positions (Dewell and Gabbiani 2018a). Next, an

127 image of the neuron and electrodes (cf. Figure 3A) was imported into ImageJ (RRID:SCR_003070),
128 the dendritic path between the electrode tips was manually traced, and the corresponding path length
129 recorded. To estimate the electrotonic distance we measured the amplitude of the back-propagating
130 action potentials (bAP) at each location and used the difference in these amplitudes. As in a previous
131 study, the differences in bAP amplitude provided a more reliable explanatory variable for distance
132 dependent effects (Dewell and Gabbiani 2018a).

133 A neuron's frequency-dependent membrane properties are characterized by its impedance
134 profile. The subthreshold impedance can be decomposed into input impedance which describes local
135 change in membrane potential at the site of an input current and transfer impedance that describes
136 change in membrane potential at remote locations after propagation through the neuron. Both input and
137 transfer impedance shape synaptic integration within dendrites. Additionally, impedance properties at
138 the site of spike initiation influence the transformation of membrane potential into spiking activity,
139 including the frequency filtering and timing of a neuron's output. If a neuron's conductance distribution
140 is uniform, then the transfer and input impedances will have similar properties. When it is not, the
141 impedance profile varies by location and transfer depends on the recording locations and the direction
142 of signal propagation (Hu et al. 2009; Vaidya and Johnston 2013).

143 To measure the impedance profile, we injected sine waves of increasing frequency called chirp
144 (or zap) currents. We recorded the injected membrane current simultaneously with the membrane
145 potential to avoid any discrepancies between the computer-generated waveform and the current
146 injected by the amplifier. The chirp currents used were identical to those described in Dewell and
147 Gabbiani (2018b). The chirp current is defined as $I(t) = I_p sin\phi(t)$, where I_p is the peak current, $\phi(t)$
148 is the phase of the sine wave, and its instantaneous frequency is defined as $f(t) = \frac{1}{2\pi}\frac{d\phi}{dt}$ (in units of
149 Hz). We generally used chirps with a duration of 20 s (sometimes 30 s, as is illustrated in Figure 3B)
150 that increased in frequency either linearly or exponentially with time. In most experiments, as well as

151 for all simulations, we used exponentially increasing chirp currents. The linear chirp started at 0 Hz
152 and was calculated as $I(t) = I_p \sin(\pi\beta t^2)$, with t being the time from the start of the chirp (in units of
153 s) and β the rate of increase in instantaneous chirp frequency (in Hz/s). The exponential chirp was
154 given by $I(t) = I_p \sin(2\pi f_0 t e^{\beta t})$, where f_0 is the initial chirp frequency and β determines the
155 (accelerating) rate of frequency increase (Barrow and Wu 2009). For all exponential chirps, we used f_0
156 = 0.05 Hz and β = 0.24 Hz which produced a chirp current increasing to 35 Hz over 20 s. We saw no
157 differences in the calculated impedance profiles with chirps having different frequency profiles, in
158 accordance with previous comparisons of impedance profiles between chirps of increasing and
159 decreasing frequencies (Ulrich 2002; Erchova et al. 2004; Hu et al. 2002; van Brederode and Berger
160 2008; van Brederode and Berger 2011) or comparison of linearly increasing chirps and sums of sine
161 wave stimuli (Hutcheon et al. 1996).

162 **Pharmacology**

163 We applied the HCN- channel blocker ZD7288 and the M-channel blocker XE991 either
164 directly in the bath saline or by local puffing as previously described (Dewell and Gabbiani 2018a,
165 2018b). For local puffing we used a micropipette connected to a pneumatic picopump (PV830, WPI,
166 Saratoga, FL). Drugs were mixed with physiological saline containing fast green (0.5%) to visually
167 monitor the affected region. For both delivery methods, drug concentrations within the lobula were
168 ~200 μM for ZD7288 and ~100-200 μM for XE991. In dual recording experiments, mecamylamine
169 was applied to block excitatory postsynaptic potentials (EPSPs) and was present in both control and
170 drug conditions. Blockade of EPSPs reduced membrane noise as well as noise in the calculated
171 impedance profiles. In paired comparisons, mecamylamine caused small increases in impedance
172 amplitude (~5%) but this difference was smaller than the variability between animals or between
173 dendritic locations. For control data we thus pooled recordings with and without mecamylamine.

174 **Experimental design and statistical analyses**

175 Data analysis was carried out with custom MATLAB code (The MathWorks, Natick, MA).
176 Linear fits were done by minimization of the sum of squared errors. Before each chirp current a -2 nA
177 hyperpolarizing step current was used for monitoring the input resistance and the membrane time
178 constant. Unless otherwise specified, all statistical tests were made using the Wilcoxon rank sum test
179 (WRS) which does not assume normality or equality of variance. Normality of the data was assessed
180 by using a Lilliefors test for any tests assuming it.

181 The complex impedance Z was calculated as $Z(f) = \mathrm{fft}(V_m)/\mathrm{fft}(I_m)$ where fft is the (frequency
182 dependent) fast Fourier transform, I_m the membrane current, and V_m the membrane potential. Both I_m
183 and V_m were down sampled to 2 kHz before the fft. Z was calculated for each trial and then averaged
184 across trials. The complex impedance is composed of its real part, the resistance R, and its imaginary
185 part, the reactance X: $Z = R + i\,X$. A positive reactance, or inductance, indicates that changes in V_m
186 precede changes in I_m. Conversely, a negative reactance, or capacitance, indicates that changes in I_m
187 precede changes in V_m. The impedance amplitude is calculated as the absolute value of Z: $|Z(f)| =$
188 $\sqrt{R(f)^2 + X(f)^2}$. The impedance phase is calculated by the inverse tangent of the reactance divided
189 by the resistance: $\Phi(f) = \tan^{-1} X(f)/R(f)$. This impedance phase is equal to the angle between the
190 x-axis and a line from the origin to a point of the impedance locus plot (cf. Figure 5C).

191 Input impedance (Z_{IN}) was calculated from the V_m and I_m recorded at the site of current
192 injection. Transfer impedance (Z_{TR}) was calculated with the I_m from the site of current injection and the
193 V_m from the non-injected site. Voltage attenuation was calculated as the relative reduction in
194 impedance amplitude from the current injection site to the non-injected site: $V_{att}(f) =$
195 $(|Z_{\mathrm{IN}}(f)| - |Z_{TR}(f)|)/|Z_{\mathrm{IN}}(f)|$. Similarly, the phase lag was calculated as the input minus the transfer
196 impedance phase. The input and transfer impedance phases were each converted to the time domain by
197 $t_{phase}(f) = \Phi(f)/(2\pi f)$ where f is the instantaneous chirp frequency (in Hz) calculated as $f(t) =$
198 $\frac{1}{2\pi}\frac{d}{dt}\sin^{-1}(\frac{I(t)}{I_p})$, for details see (Dewell and Gabbiani 2018b). The mean V_m delay was then calculated

199 by averaging across frequencies the absolute value of the delay between the input current and
200 membrane potential.

201 Resonant strength was calculated from the input impedance amplitude as the ratio of the
202 maximum impedance to the steady state (0 Hz) impedance. The impedance frequency variation (f_{var})
203 was calculated as the standard deviation (across frequencies ranging from 0 to 35 Hz) of the impedance
204 amplitude profile divided by the mean impedance amplitude. Unlike resonance strength, f_{var}
205 incorporates both the strength and breadth of the bandpass, giving an indication of how ohmic (or
206 broadband) the membrane is. Indeed, an ideal resistor would have a frequency variation of zero while a
207 membrane exhibiting sharp bandpass attributes would produce high frequency variation. The
208 membrane constant values used for our electrical circuit models yielded f_{var} values of 18.4 for the
209 lowpass circuit, and 378 for the strongest bandpass circuit (see below; Fig. 4G). There is a potential
210 drawback to the statistic, though, since it depends on the frequency range examined, limiting the ability
211 to compare values between studies examining different frequency ranges.

212 For calculating the power density of the membrane potential, we used the Matlab multitaper
213 power spectral density estimate (function 'pmtm'), with a time-half bandwidth product of 4 measured
214 over 15 octaves at frequencies of 2^{-4} to 2^{11} Hz with 8 voices (scales) per octave. The mean was
215 subtracted from all data before calculating the power density estimate and the resulting estimates were
216 then averaged across trials. For estimating the time-varying power density we used Matlab's
217 continuous wavelet transform (function 'cwt'). The frequency range was set from 0.1 to 2,000 Hz and
218 the signal was not extended. As for the spectral density estimate, wavelet transforms were calculated
219 for individual trials and the resulting wavelet transform coefficients were then averaged across trials. In
220 the calculation of both measures, the raw data was used with no down sampling or filtering.

221 **Electrical circuit model**

222 The LGMD membrane impedance was compared to the impedance of an equivalent cable
223 based on a series of either RC or RLC circuits. RC circuits describe passive membranes, while RLC

224 circuits can approximate the frequency-dependent properties of active neuronal membranes. Active
225 conductances are both frequency and voltage dependent, while inductances are only frequency
226 dependent. The RLC circuit was modeled as illustrated in Figure 4F. The membrane impedance density
227 was calculated as:

228 $$Z_m = \frac{R_m}{1 - l_{rat} + l_{rat}/(1 + i\tau_L\omega) + i\tau_m\omega}$$

229 where Z_m is the input impedance density (in units of Ωcm^2), R_m is the membrane resistivity (Ωcm^2), C_m
230 is the membrane capacitance (F/cm^2), τ_m (s) is membrane time constant ($\tau_m = R_m C_m$), τ_L is the
231 inductance time constant (s), ω is frequency in rad/s, l_{rat} is the ratio of the membrane conductance that
232 is in series with the inductor (range [0–1]), and $i = \sqrt{-1}$. If l_{rat} is zero, then no current will pass through
233 the inductor and the circuit is equivalent to an RC circuit with membrane impedance:

234 $$Z_m = R_m/(1 + i\tau_m\omega).$$

235 In both cases, the input impedance (Z_{IN}) was calculated by dividing Z_m by the unit surface area of the
236 cable (cm^2). We used the average dendritic circumference of our full LGMD model (20.85 µm) for the
237 cable circumference.

238 Transfer impedance measures were based upon a cable of fixed diameter and infinite length.
239 The voltage transfer along the cable was calculated as $V_{TR} = e^{-l/\lambda}$, where l (cm) is the distance
240 between the two locations and λ is the cable's length constant (cm), $\lambda = \sqrt{Z_m/(R_a d b_f)}$. R_a is the axial
241 resistivity (Ωcm), d is the diameter (cm), and $b_f = 3$ is the branch factor – a scalar added to account for
242 additional attenuation due to the dendritic branching. The transfer impedance Z_{TR} at distance l from the
243 site of current injection is the product of Z_{IN} and V_{TR}.

244 **Morphological neuron models**

245 Comparisons between different cell morphologies used published neuron models downloaded
246 from ModelDB (RRID:SCR_007271) and a simplified Rall model (Rall 1964). The Rall model
247 (illustrated in Fig. 1) had 64 sections, each 20 µm long. The soma had a 20 µm diameter and the

248 dendritic arbor had 5 branch levels. The base branch had a 12 μm diameter with each level decreasing
249 in diameter according to the 2/3 power law (Rall 1964). Among the available morphologies, we
250 selected neurons spanning a wide range of branching patterns and sizes. The morphologies used
251 included a cerebellar Purkinje neuron (Miyasho et al. 2001; Ostojic et al. 2015), a CA1 pyramidal
252 neuron (Migliore et al. 2004), an oriens-lacunosum/moleculare (OLM) hippocampal interneuron
253 (Sekulić et al. 2015), and a human layer 2/3 temporal cortex pyramidal neuron (Eyal et al. 2016). As
254 we sought to compare the influence of the cell morphology, all models were passive with identical
255 membrane properties close to those used in the LGMD model (C_m = 0.8 μF/cm^2, G_m = 0.1 mS/cm^2, Ra
256 = 350 Ωcm). All simulations were carried out using the NEURON software simulation package. For a
257 passive model measuring impedance with chirp currents, as was done experimentally, or with
258 NEURON's built-in impedance tools yielded the same result, so we used the built-in impedance
259 measurement to speed up the simulations carried out for Fig. 8A and B.

260 In Fig. 8G, the percentage of cell surface area with improved transfer impedance amplitude was
261 calculated from the data depicted in Fig. 8F (right). Specifically, we calculated the transfer impedance
262 amplitude between all neuron segments and compared it to the impedance amplitude of an isopotential
263 model (using the same cell morphology but with axial resistivity set to zero). The impedance amplitude
264 of an isopotential cell is $R/(1 + \tau_m^2\omega^2)^{0.5}$, where R is the membrane resistance (MΩ), ω is the frequency
265 (s^{-1}), and τ_m is the membrane time constant (s). As C_m and G_m were the same for all morphologies, their
266 membrane time constants were the same ($\tau_m = C_mG_m$) while the membrane resistance changed with
267 their total membrane area A ($R = (AG_m)^{-1}$). For each segment, we summed the surface area of all
268 segments to which a broadband signal transferred with greater gain than the isopotential value (dashed
269 line in Fig. 8F, right) and divided by the neuron's total surface area. Frequencies of 0 to 1,000 Hz were
270 used and averaged with equal weight.

271 Similarly, to obtain Fig. 8I we compared the transfer impedance phase between all segment
272 pairs and compared it to the impedance phase of an isopotential equivalent. The impedance phase of an

273 isopotential cell is $\tan^{-1}(-\tau_m \omega)$, as illustrated in Fig. 1B, right. For the phase measurements, a weighted
274 average was used with the transfer amplitude between the segment pair determining the weight for
275 each frequency. As signals of some frequencies transfer better than others, the transfer phase of these
276 signals influences the membrane synchrony more. The percentage area with increased impedance
277 phase was then calculated by summing the surface area of segments with more synchronous transfer
278 phase than an isopotential equivalent cell and dividing by the total membrane surface area of the
279 neuron. These calculations effectively measure the average signal transfer of a passive cell with
280 realistic morphology under the simplifying assumptions that broadband inputs impinge upon the
281 neuron with a uniform density. Although these assumptions would not necessarily hold *in vivo* where
282 the locations and frequency of inputs is constantly changing, they provide a method of estimating
283 transfer impedance without relying on the less realistic assumptions that all inputs impinge on a single
284 location or that all signals only integrate at a single location, like the neuron's spike initiation zone.
285

286 ## Results

287 **Broader impedance profiles improve the discrimination of input timing.** The input impedance
288 (Z_{IN}) of passive neurons can be approximated by RC circuits containing a parallel capacitance and
289 resistance. It is well known that such circuits exhibit a sharp lowpass filtering of input currents. If a
290 sinusoidal current is applied to an RC circuit or a passive neuron, then higher frequencies produce
291 smaller changes in membrane potential resulting in a frequency dependent gain (Fig. 1A). The
292 impedance phase similarly decreases with input current frequency (Fig. 1B). The slower the
293 membrane, or equivalently the higher the membrane time constant, the faster gain and phase decay
294 with frequency. Conversion of the impedance phase to time shows that the delay between an input
295 current and the resulting change in membrane potential is equal to τ_m for low frequencies (Fig. 1C).
296 This Z_{IN} delay decreases with increased signal frequency. Long, frequency dependent delays reduce the
297 ability of neurons to discriminate between synaptic input arrival times. To prevent this, auditory

298 neurons that precisely discriminate the timing of their synaptic inputs have small time constants (~0.3
299 ms), thereby minimizing the delay between input currents and change in V_m (McGinley et al. 2012;
300 Mikiel-Hunter et al. 2016; Remme et al. 2014).

301 Simulations with model CA1 pyramidal neurons show that g_H increases the ability of a neuron
302 to discriminate the timing of its synaptic inputs (Migliore et al. 2004). In such simulations, a barrage of
303 synaptic inputs impinges on randomly selected dendritic branches with varying degrees of synchrony.
304 The input synchrony is altered with the addition of a random temporal jitter applied to each input.
305 Replacing g_H by an inductance results in a similar increase in synchrony discrimination. To
306 demonstrate this, we simulated 100 synaptic inputs impinging with varying degrees of synchrony onto
307 an artificial model neuron (Fig. 1D; Rall model, Methods). In the passive case, lowpass filtering
308 prevented discrimination of input synchrony (Fig. 1D, blue line). Furthermore, the spike timing was
309 less reliable and had a longer latency (Fig. 1E, blue line). As in the CA1 model simulations, active
310 dendritic conductances, in this case g_H and g_M, increased the discrimination of the input synchrony and
311 produced spikes with shorter, more consistent latencies (Fig. 1D and E, black). Replacing these
312 conductances with an inductance resulted in the exact same increase in input synchrony discrimination
313 with slightly improved spike timing, illustrating the role played by g_H and g_M's phenomenological
314 inductance (Fig. 1D and E, red).

315 Among these three models, the passive Rall branching model is the most effective low-pass
316 filter (Fig. 1F,G, blue). The active conductance and the inductance models differ slightly, but share key
317 similarities (Fig. 1F,G). In both models the gain and phase decrease less with frequency than in the
318 passive case, reducing lags at low frequencies. We quantified these two points by computing the
319 frequency variation (Fig. 1H) and the mean V_m delay (Fig. 1I). Earlier work showed that
320 discriminating between temporal patterns of excitatory inputs is key to the LGMD's selectivity for
321 looming stimuli (Jones and Gabbiani 2010). What then is its impedance profile, and can it explain
322 synaptic pattern discriminability in the LGMD?

323 **The spectral power density of the LGMD's membrane potential is concentrated at low**
324 **frequencies.** The LGMD possesses three dendritic fields with the largest one, field A, integrating
325 excitatory inputs originating from every facet of the compound eye (Fig. 2A). It responds more or less
326 vigorously to approaching objects that activate thousands of facets based on the object's trajectory and
327 spatial coherence (Dewell and Gabbiani 2018a; Gray et al. 2001). Currently, it is unknown what
328 synaptic input current frequencies most neurons experience *in vivo*. To address this question, we first
329 measured the power spectrum of the membrane potential for spontaneous activity. The LGMD receives
330 a high number of spontaneous synaptic inputs (Fig. 2D; Jones and Gabbiani, 2012) and its membrane
331 time constant is short *in vivo* (~ 7 ms; Gabbiani and Krapp, 2006; Peron et al., 2007; Dewell and
332 Gabbiani, 2018a, 2018b). This raises the possibility that high frequency components might dominate
333 the LGMD's membrane potential power spectrum. However, we found that 87% of the power was
334 contained below 35 Hz, with 50% at less than 7.5 Hz (Fig. 2E, black lines).
335 Next, we computed the spectral power density in response to looming stimuli. During the
336 course of such a stimulus the number of activated ommatidia increases from ~10 to over 2,500,
337 producing an increase in activated synapses from ~100 to over 20,000 (Rind et al. 2016). As this
338 increased synaptic input occurs in ever tighter time windows (Fig. 2C), it might lead to a shift in power
339 towards higher frequencies. However, low frequency power increased during looming stimuli, with
340 over 50% of it below 1.5 Hz (Fig. 2E, blue lines). As most of the membrane depolarization and spiking
341 activity generated by looming occurs over the last second before collision, we also used wavelet
342 analysis to resolve the frequency content of the membrane potential in the time domain (see Methods).
343 During this period there was an increase in power spectral density at higher frequencies (Fig. 2F, gray
344 box), but most power remained centered around 1-2 Hz (Fig. 2F). The concentration of the LGMD
345 membrane potential power at low frequencies despite high frequency synaptic input could be due to
346 the activation characteristics of these inputs or to low-pass filtering by the LGMD's membrane. We
347 tested the latter possibility by measuring the frequency-resolved input and transfer impedance of the

348 LGMD's membrane. The input impedance reveals the mapping of current to local dendritic membrane
349 potential frequencies, while the transfer impedance documents the change in membrane potential
350 frequency content as the signal propagates from the dendrites toward the SIZ.

351 **Single and dual dendritic LGMD recordings *in vivo* in response to chirp currents.** The LGMD's
352 input and transfer impedance were measured by recording *in vivo* the membrane potential with sharp
353 electrodes (Fig. 3A). These experiments consisted of injecting chirp currents (sine waveforms with
354 time-varying frequency) during single or paired recordings in the excitatory dendritic field (see
355 Methods). Superposing chirp currents on different holding currents allowed us to measure impedance
356 at multiple steady-state membrane potentials (V_{ss}; Fig. 3B), and thus at different steady-state activation
357 levels of subthreshold conductances present in the LGMD membrane. In general, chirp responses
358 looked consistent across V_{ss} values, tapering slightly with increasing frequency. Examination of
359 different periods of the chirp show that at low frequencies the oscillations in membrane current and
360 potential were synchronous, while at higher frequencies the membrane potential lagged behind the
361 current and the change in potential was smaller (Fig. 3C). We conducted similar experiments in
362 voltage clamp and found similar changes to occur (Fig. 3D).

363 Quantification of transfer impedance characteristics was made as a function of the distance
364 between different pairs of dendritic recordings. The inter-electrode distance was measured both as the
365 dendritic path length between the electrodes in experimental micrographs (path distance, Fig. 3A), and
366 as the difference in back propagating action potential (bAP) amplitudes (electrotonic distance). At the
367 base of the excitatory dendritic field, the bAP amplitude was ~40 mV and decayed to <10 mV in distal
368 dendritic branches. The recording locations in the present study were in larger branches with bAP
369 amplitudes between 20 and 40 mV. The path distances between these electrode pairs ranged from 63 to
370 150 μm. The difference in bAP amplitudes was well correlated with changes in membrane potential
371 transfer properties (Fig. 3E). In contrast, there was no correlation between path distance and voltage
372 attenuation ($r(9) = 0.17$, $p = 0.63$, Pearson linear correlation), likely due to differences in dendrite

373 diameter or number of branch points between the recording pairs. With increased electrotonic distance
374 between recording pairs, there was reduced voltage transfer and an increased delay. The closest
375 recordings had ≤10% voltage attenuation, while for more distant pairs this value increased to almost
376 50% (Fig. 3E). The average phase and time lags between locations were ~3° and 0.5 ms between the
377 most synchronous pairs and ~10° and 2 ms between the most asynchronous pairs. For subsequent
378 analyses of transfer impedance, data from all recording pairs were pooled.

379 **Consistency of impedance amplitude across holding potentials and chirp frequencies.** The
380 impedance amplitude is the absolute value of the complex impedance and represents the gain function,
381 mapping at each frequency a given synaptic or electrode current into a change in membrane potential.
382 We measured the impedance amplitude at different V_{ss} values and examined how its profile changed
383 with holding potential. The LGMD dendrites have a resting membrane potential near -65 mV, can be
384 hyperpolarized by inhibitory inputs to below -70 mV, and are depolarized by excitatory inputs to >-50
385 mV during looming stimuli (Fig. 2C). We thus used V_{ss} values spanning that range and confined below
386 the spike threshold potential.

387 Input impedance amplitude was highest at low membrane potentials (<-75 mV), particularly at
388 low frequencies (Fig. 4A, dashed box). Yet, despite the LGMD's resting HCN and M conductances
389 (Dewell and Gabbiani 2018a, 2018b) changes in V_{ss} produced little change in impedance amplitude
390 (Fig. 4A). This differs from other HCN and M channel-expressing neurons that exhibit a pronounced
391 resonant frequency (Gastrein et al. 2011; Gutfreund et al. 1995a; Hu et al. 2002; Hutcheon et al. 1996).
392 The transfer impedance amplitude similarly changed little with membrane potential and tapered only
393 slightly with increased frequency (Fig. 4B). Accordingly, the voltage attenuation between paired
394 recording locations also showed a high overlap across holding potentials (Fig. 4C). The variability of
395 the voltage attenuation between recording pairs was higher though, due to the differences in
396 electrotonic distance (Fig. 3E). The constancy of impedance amplitude at different V_{ss} values implies a
397 constant total membrane conductance across holding potentials. While other channel types might

398 contribute, HCN and M channels account for the majority of the LGMD's resting membrane
399 conductance, suggesting that their total conductance remains roughly constant. This in turn would
400 increase the consistency of EPSP amplitudes across holding potentials. This idea was confirmed by
401 injecting currents simulating EPSP waveforms at the same V_{ss} values used to measure impedance,
402 resulting in peak depolarizations that were independent of V_{ss} ($r(89) = -0.05$, $p = 0.63$, 91 V_{ss} values
403 from 16 recordings in 9 animals).

404 The resonance properties of an electrical circuit are characterized by its bandwidth and
405 resonance strength (the Q factor, Horowitz and Hill, 2015). However, neuronal membranes have
406 complex impedance profiles that are not as easily characterized. The most commonly used measure of
407 neuronal resonance strength is the ratio of peak to steady-state (0 Hz) impedance (Koch 1984a).
408 Unfortunately, this measure ignores impedance at other frequencies. So, in addition to this standard
409 measure (see below, Fig. 6H), we wanted an additional measure that incorporated impedance at
410 frequencies below and above the resonant frequency and thus we characterized the variability of the
411 impedance amplitude by its standard deviation across frequencies normalized to the mean impedance
412 amplitude, which we call the frequency variation (see Methods). The frequency variation of the
413 LGMD's input impedance amplitude was 10-15% and decreased slightly with membrane
414 depolarization (Fig. 4D, black). Transfer impedance amplitude had a frequency variation of ~20% and
415 also decreased with depolarization (Fig. 4D, red). The power spectral density at 0 Hz was 1,000-fold
416 higher than at 35 Hz during looming stimuli and 25-fold higher during spontaneous inputs (Fig. 2E).
417 For the same frequencies, both the input and transfer impedance amplitudes were less than 2-fold
418 higher. For comparison, if the synaptic inputs during looming were broadband and the lowpass spectral
419 density were due to membrane filtering, this would imply a frequency variation >250%. The lack of
420 prominent lowpass filtering rules out the membrane impedance as the cause of the power spectrum
421 concentration at low frequencies (Fig. 2E,F). Instead, this suggests that the low frequency power is due
422 to the activation characteristics of the synaptic input currents during a looming stimulus.

423 To test what electrical components could produce the impedance amplitude properties of the
424 LGMD, we created an array of RC and RLC circuit models (Fig. 4E, F), as in earlier studies (Koch
425 1984b; Mauro 1961; Rall 1964). For both model types we used a specific membrane capacitance (C_m)
426 and conductance (G_m) yielding a time constant (τ_m) of 6.9 ms, close to that measured experimentally in
427 the LGMD (Dewell and Gabbiani 2018a, 2018b; Gabbiani and Krapp 2006a; Peron et al. 2007a). The
428 RLC circuit contained, in addition to the parallel conductance and capacitance, a series conductance
429 and inductance to account for the effects of restorative membrane conductances like g_M and g_H (Fig.
430 4F). We varied the percentage of G_m that was in series with the inductance and the inductance time
431 constant (τ_L) to determine which, if any, parameters reproduced the LGMD's impedance amplitude.
432 These two parameters then model the percentage of the membrane conductance passing through the
433 active channels and the time constant of the active conductance. For most of the tested parameter
434 space, the circuit model's input impedance amplitude varied more with frequency than that of the
435 LGMD (Fig. 4G). Circuits with a fast inductance (≤ 10 ms) had impedance amplitudes as consistent as
436 that of the LGMD, while slow inductances increased the frequency variation beyond that of an RC
437 circuit, which was already higher than that of the LGMD. This is surprising considering that the
438 LGMD's resting membrane conductance is heavily dependent on rectifying HCN channels with a time
439 constant of ~1 s (Dewell and Gabbiani 2018a). To assess the importance of the LGMD's membrane
440 time constant to the frequency variation, we examined the same range of inductance values in an RLC
441 circuit with doubled τ_m (increasing τ_m by increasing C_m or by decreasing G_m had the same effect). With
442 the higher τ_m, no inductance parameters produced a frequency variation as low as that of the LGMD.
443 Therefore, the low frequency variation of the LGMD's impedance profile depends on a fast τ_L in
444 addition to the fast τ_m. Of the LGMD's known conductances, g_M is the most likely candidate to provide
445 such a fast inductance.

446 **Impedance phase reveals high current – voltage synchrony across membrane potentials.**

447 Membrane capacitance produces a phase lag between input currents and their resulting change in

448 membrane potential that increases both with frequency and distance of propagation. Conductances like
449 g_H and g_M counteract this lag and increase the synchrony between synaptic input currents and the
450 membrane potential (Hu et al. 2009; Narayanan and Johnston 2008; Ulrich 2002; Vaidya and Johnston
451 2013). To characterize the timing of the LGMD's membrane potential with respect to current inputs,
452 we thus measured the frequency-dependent dendritic impedance phase. In a passive, isopotential
453 neuron, membrane capacitance forces input impedance phase to saturate at -90° as input current
454 frequency increases (Mauro 1961; Narayanan and Johnston 2008). Conversely, a positive impedance
455 phase indicates that the change in voltage precedes the change in current, a feature requiring a
456 physiological process that resembles an electrical inductance. Like impedance amplitude, the LGMD's
457 impedance phase varied little with V_{ss} values, distinguishing it again from other neurons (Gutfreund et
458 al. 1995a; Narayanan and Johnston 2008). For all holding potentials, the phase was positive at low
459 frequencies (≤ 1 Hz). Although phase decreased with frequency, it saturated well above -90° and in
460 some recordings even increased at frequencies > 20 Hz. This was the case for both the input and the
461 transfer impedance phase (Fig. 5A and B, respectively). The LGMD subthreshold membrane potential
462 exhibited zero phase and hence was most synchronous with input current at ~1 Hz, in contrast to
463 spiking which is most synchronous with input currents of ~6 Hz (Dewell and Gabbiani 2018b).
464 Plotting as in Fig. 5C the real and imaginary components of the input impedance, called
465 respectively resistance and reactance, illustrates both the low frequency inductive and the high
466 frequency capacitive properties of the input impedance phase (corresponding to positive and negative
467 reactance, respectively). Such impedance locus plots combine the information on the impedance
468 amplitude (Fig. 4A) and phase (Fig. 5A): for each point in a locus plot if one were to draw a line
469 segment from the origin to the point, the length of the segment would be equal to the impedance
470 amplitude and the angle relative to the x-axis is the impedance phase. Fig. 5C confirms that the input
471 reactance was consistent across V_{ss} values while the input resistance increased at hyperpolarized
472 potentials resulting in a rightward shift of the curves as V_{ss} decreased. The impedance locus plot of the

473 transfer impedance reveals even less change across membrane potentials, with only a small increase in
474 transfer resistance at hyperpolarized potentials (Fig. 5D). The relative phase of the input and transfer
475 impedances is the membrane potential phase lag with larger values indicating increased transfer delay
476 (Fig. 5E). The phase lag between input and transfer phase was also consistent across V_{ss} values and
477 was negative at frequencies ≤ 1 Hz, indicating an inductive phase shift on the propagating membrane
478 potential. The low frequency inductive characteristics of both the input and transfer impedance reveal
479 the influence of a slow inductor, consistent with the presence of a slowly rectifying HCN conductance.
480 Signal frequencies with zero reactance (and therefore an impedance phase of zero) have no
481 delay between membrane current and potential. On average, the LGMD's membrane potential and
482 current were offset by ~2 ms at the input location independent of V_{ss} (Fig. 5F, grey). The mean delay
483 of the transfer impedance was ~3 ms at V_{ss} near -80 mV and decreased with depolarization (Fig. 5F,
484 red). We similarly measured the delay between membrane potentials recorded at two positions, which
485 was ≤ 1 ms (Fig. 5F, brown). To test how this measured timing compared to that of an RLC circuit, we
486 surveyed the same parameter range as depicted in Figure 4. No inductance parameters generated a
487 circuit as synchronous as the LGMD. Circuits with a large and fast inductance generated the lowest
488 input impedance delay, but this was still > 3.5 ms (Fig. 5G). Reproducing the LGMD's low frequency
489 inductive phase (Fig. 5A,B) required an RLC circuit model with a slow inductance ($\tau_L \approx 1$ s). The
490 dashed black lines of the low frequency insets (Fig. 5A,B & D) were produced by inductance
491 parameters marked by the black star in Fig. 5G. Although the addition of a slow inductance to an RLC
492 circuit reproduced the low frequency inductance of the LGMD membrane, it increased the input and
493 transfer asynchrony of the circuit model further from that of an RC circuit (Fig. 5H). In contrast, the
494 asynchrony between the membrane potential recorded at the two locations could be reproduced by
495 either cable model (Fig. 5H, right). This shows that the LGMD must have an additional synchronizing
496 influence unaccounted for by the circuit model. Whether this increased synchrony is explainable by the
497 LGMD's active membrane conductances is not immediately evident.

498 **HCN and M channels reduce impedance amplitude and frequency variation.** To assess the
499 influence of HCN and M channels on the LGMD's input impedance profile, we measured the input
500 impedance before and after addition of two channel specific blockers: ZD7288 and XE991,
501 respectively. Blocking g_H reduces the resting membrane potential and input resistance of the LGMD
502 (Dewell and Gabbiani 2018a), so after HCN blockade we applied chirps with lower peak current and
503 higher holding current to generate equivalent V_{ss} values and changes in membrane potential (Fig. 6A).
504 After g_H blockade a decrease in the membrane potential was seen with increasing chirp frequencies.
505 The impedance amplitude doubled at low frequency and decreased more steeply with input frequency
506 (Fig. 6B). A reduction in inductance was also clear from the decreased impedance phase (Fig. 6C).
507 Blockade of g_M increases the LGMD's resting membrane potential and input resistance (Dewell
508 and Gabbiani 2018b), so we used decreased holding currents and chirp amplitudes after blockade to
509 account for these changes. After g_M blockade, a resonance emerged (Fig. 6D, arrowhead). This was
510 reflected in the peak near 4 Hz in the impedance amplitude profile (Fig. 6E). This resonance likely
511 helps generate the increased spiking observed in response to ~4 Hz current inputs following g_M
512 blockade (Dewell and Gabbiani 2018b). The impedance phase increased at frequencies ≤ 2 Hz and
513 decreased at higher frequencies (Fig. 6F). These effects suggest that in addition to implementing an
514 inductance evident above 2 Hz, g_M also counteracts an additional inductance that increases impedance
515 amplitude at frequencies around 4 Hz and phase at frequencies ≤ 2 Hz.
516 Both g_M and g_H reduced frequency variation, causing a larger reduction at depolarized and
517 hyperpolarized potentials, respectively, consistent with their activation kinetics (Fig. 6G). The
518 increased frequency variation after block of either channel was due to a large increase in the range of
519 resistance across frequencies and a reduced high frequency reactance. We also calculated the
520 resonance strength, a common measure of how bandpass a membrane is, and found it to be small at all
521 V_{ss} values in control conditions and after g_H block (Fig. 6H, black and red). After g_M block, though, at
522 resting V_m and above a strong membrane resonance was observed with impedance amplitude around 4

523 Hz double that of steady state (0 Hz; Fig. 6H, green). Both conductances contribute to decrease the
524 membrane impedance amplitude of the LGMD, with g_H causing the largest reduction at and below
525 resting Vm and g_M at depolarized potentials, respectively. Although we did not measure the effects of
526 g_H and g_M blockade on transfer impedance, input and transfer resonance were similar in control
527 conditions (with resonant strengths differing by < 0.05 for >75% of trials). So, the changes in transfer
528 resonance after channel block would most likely parallel those of input resonance.

529 In addition to reducing the impedance amplitude and making it more consistent across
530 frequencies, both g_H and g_M decreased the delay between input current and the resulting change in
531 membrane potential. After blockade of either channel the input delay increased, with g_M blockade
532 having the largest effect (Fig. 6I). After g_M blockade the minimum phase was more capacitive at high
533 frequencies and the maximum phase more inductive at low frequencies (Fig. 6F). After g_H blockade,
534 the input impedance phase decayed to a minimum at a lower frequency (Fig. 6C). The decrease in
535 input impedance delay produced by g_H and g_M would improve the LGMD's ability to discriminate the
536 timing of its synaptic inputs (see below), but even after blocking the channels, the delay between I_m
537 and V_m was still smaller than any RLC circuit model (compare Fig. 6I and Fig. 5H). This suggests that
538 there must be an additional mechanism beyond these membrane conductances that further reduces
539 these delays, as confirmed by investigating the impact of neuronal morphology (see below).

540 **Pronounced effect of g_M on temporal input discrimination.** We have previously shown that
541 blockade of g_H reduced the LGMD's ability to discriminate the spatial pattern of its synaptic inputs
542 (Dewell and Gabbiani 2018a), but the role of the LGMD's active conductances in discriminating
543 temporal patterns has not been addressed. We tested this with the same sort of simulations described in
544 Figure 1, using a full LGMD model that reproduces most of its experimental properties (Dewell and
545 Gabbiani 2018a, 2018b). Increased noise in the timing of synaptic inputs quickly reduced spiking (Fig.
546 7A, black). Simulations conducted without g_H slightly reduced the model's sensitivity to input timing,
547 but g_M's removal created a substantial reduction (Fig. 7A). The removal of both conductances

548 decreased the ability to discriminate between input timings by over half (Fig. 7A, blue). These changes
549 in spike probability were accompanied by similar effects on spike timing. Removal of g_M increased the
550 spike latency (measured from the start of synaptic excitation) as well as its variability (Fig. 7B). This
551 confirms previous experimental findings on the importance of g_M in spike timing precision (Dewell
552 and Gabbiani 2018b). In the LGMD, g_H plays a critical role in the discrimination of synaptic input
553 patterns during prolonged excitation (Dewell and Gabbiani 2018a), but the present simulations indicate
554 that it does not play a similar role for brief periods of synaptic excitation.

555 **Neuronal morphology increases membrane gain and high frequency synchrony.** To test the
556 influence of morphology on membrane impedance we compared simulations between passive models
557 that were either isopotential or had realistic branching and attenuation. These simulations build upon
558 earlier ones that examined the role of morphology on signal propagation and impedance in other
559 neurons (Holmes et al. 1992; Jaffe and Carnevale 1999; Mainen and Sejnowski 1996; Vetter et al.
560 2001). The principal difference in the current simulations is the characterization of morphological
561 influence on the impedance delay and calculation of the net influence of morphology on input currents
562 distributed throughout the dendritic arbors.

563 Plotting the input impedance delay of every section of the full LGMD model (Fig. 8A) revealed
564 that it was reduced from that of an isopotential model (dashed line) indicating higher synchrony
565 between a local input current and membrane potential. For the same frequency range used in
566 experiments, the passive model segments had a mean input delay of 2.1 ± 1.1 ms, matching
567 experimental data (c.f. Fig. 5H). This suggests that the LGMD morphology plays a bigger role in the
568 membrane potential's delay relative to input current than its active conductances. The input impedance
569 amplitude was also altered by cell morphology, decreasing less with frequency than in an isopotential
570 equivalent model (Fig. 8B; solid vs. dashed lines). The input frequency variation of the model sections
571 was 8.6 ± 4.7% for the physiologically dominant frequency range (< 35 Hz; see Fig. 1), demonstrating

572 that the LGMD's morphology alters the input impedance amplitude profile as much as its active
573 conductances. At higher frequencies, the input impedance amplitude remained monotonically
574 decreasing, but was always higher than that of the isopotential model (Fig. 8B, dashed line).

575 To determine whether the effects of morphology on impedance was unique to the LGMD, we
576 conducted similar simulations using four other neuronal morphologies covering a range of sizes and
577 branching patterns (Fig. 8C). The additional morphologies examined were taken from cerebellar
578 Purkinje, layer 2/3 pyramidal, CA1 pyramidal, and oriens-lacunosum moleculare (OLM) neurons. The
579 membrane conductance and capacitance were uniform and the same for all models producing a
580 membrane time constant of 8 ms. Simulations with slower τ_m yielded qualitatively similar results. For
581 all morphologies, input impedance delay decreased (Fig. 8D) and amplitude increased (Fig. 8E)
582 relative to their isopotential equivalents (otherwise identical models with zero axial resistance).

583 Hence, the branched structures of the LGMD and other neurons enhance local inputs with
584 increased gain and higher synchrony between input currents and changes in membrane potential. This
585 is offset in part by lower signal transfer because the branching and axial resistance also increase
586 voltage attenuation between cell regions. The net effect of the morphology on the membrane
587 impedance is therefore not immediately apparent. In experiments, transfer impedance was measured by
588 injecting current at a single location and recording the membrane potential at another. Synaptic
589 currents, however, impinge at thousands of locations spread out across the dendrites. Furthermore,
590 these inputs don't propagate independently to the site of spike initiation.

591 The precise effect of morphology on synaptic integration depends on the pattern of its inputs,
592 which are unknown for most neurons, so we assumed broadband inputs spread across the entire arbor.
593 To assess the net effect of morphology on impedance we thus calculated the transfer impedance in an
594 all-to-all manner, with current frequencies between 0 and 5 kHz injected successively into each model
595 segment and the impedance measured in all other segments of the model. An example of transfer
596 impedance profiles from one dendritic segment of the LGMD is illustrated for a 35 Hz current in Fig.

597 8F (delay on left, amplitude on right). These plots show that segments near the current injection site
598 (arrowheads) had higher transfer impedance while more distant segments had lower transfer
599 impedance than an isopotential equivalent (dashed lines). For all segments of all models, at all
600 frequencies, nearby segments exhibited increased and distant segments decreased transfer impedance
601 relative to the isopotential models. To determine how far signals propagated before the increased
602 attenuation overcame the increased input impedance, we quantified, for each segment, its area of
603 increased transfer impedance relative to an isopotential equivalent. This was recorded as the
604 percentage of membrane for which transfer amplitudes were higher and delays shorter compared to the
605 equivalent isopotential model. In Fig. 8F, this percentage would correspond to the surface area of the
606 segments marked in brown divided by the total membrane area (brown and black).

607 For currents injected into some LGMD segments, the surface area with increased transfer
608 amplitude was as high as 90% and amounted to ~70% for the average segment (Fig. 8G, black). The
609 Purkinje model had a similar area of increased transfer as the LGMD, while models of the pyramidal
610 and OLM neurons, however, had an increased transfer amplitude from most segments to ~90% of the
611 neuron's surface area (Fig. 8G). In addition to quantifying the area of improved transfer, we also
612 calculated membrane area weighted averages of the transfer amplitude to examine the net effect of the
613 morphology on signal transfer. Examination of the net transfer amplitude at different frequencies
614 showed that each morphology generated a bandpass increase in transfer amplitude (Fig. 8H). The CA1
615 pyramidal model had the highest increase, with 40 Hz inputs increasing by 9%. The LGMD and
616 Purkinje morphologies generated smaller increases, 4-5%, shifted at higher frequencies near 65 Hz.
617 This shows that the branching morphologies of neurons provide a bandpass increase to the overall
618 membrane gain. As branched morphologies cause membrane potentials to attenuate, it would not have
619 been surprising if their net effect were a reduced transfer amplitude relative to an isopotential model,
620 but this was not the case.

For all morphologies, the reduction in input delay was partially offset by the increase in transfer delay. The improved timing of the input impedance spread throughout most of the neurons, and the lower transfer delay propagated to almost the same membrane area as did the increased transfer amplitude (Fig. 8I). To calculate the total transfer delay, values were weighted by the strength of the transfer amplitude: if there is minimal signal transfer between 2 segments then the timing of that transfer is less relevant. The net impact of morphology on the average transfer delay was small (≤ 0.3 ms for all frequencies; Fig. 8J). All morphologies had slightly smaller net transfer delays than an isopotential equivalent model for signals above 100 Hz. The amount of this improvement scaled with the τ_m used for simulations; simulations with $\tau_m = 16$ ms had twice the improvement in delay due to morphology. The overall effect of the morphologies on transfer timing was minimal on low frequency signals, but could improve the timing of high frequency signals, like those generated from fast synaptic currents.

Discussion

Here we have described the impedance properties of the LGMD *in vivo*, measured over the range of frequencies encompassing most of the signal power mediated by the LGMD's synaptic inputs. We found that the membrane impedance amplitude of the LGMD is consistent over the range of subthreshold membrane potentials and input frequencies involved in the detection of approaching objects. Further, the membrane impedance revealed small delays between input current and resulting changes in membrane potential. This membrane timing and gain consistency were both shaped by the conductances g_H and g_M, as well as the neuron's branching morphology. Extensive modeling revealed that these changes to the LGMD's impedance profile increase its ability to discriminate the temporal patterns of excitatory synaptic inputs.

Despite a high rate of spontaneous and stimulus-evoked synaptic inputs due to the large number of excitatory synapses the LGMD receives (Rind et al. 2016), most of its membrane power was concentrated at low frequencies (Fig. 2E). During looming stimuli, as the rate of excitation increased,

646 the dominant signal frequency actually decreased with over 50% of the membrane potential spectral
647 power below 1.5 Hz (Fig. 2E, F). As neither the input nor the transfer impedance amplitude of the
648 LGMD were lowpass over the same frequency range (Fig. 4A, B), this must reflect the characteristics
649 of pre-synaptic inputs to the LGMD. Neither the membrane gain, nor the delay between I_m and V_m
650 changed dramatically over the frequencies tested, favoring integration over a broad frequency range
651 during looming.

652 To determine what shapes the frequency dependence of the impedance gain we used
653 pharmacological manipulations and computational modeling. We found that the neuron's morphology
654 and the active conductances g_H and g_M (Fig. 6G) dramatically reduced frequency variation of the
655 impedance gain, making the LGMD membrane impedance more broadband. This was surprising, as
656 both g_H and g_M usually make neurons more bandpass (Hönigsperger et al. 2015; Hu et al. 2009;
657 Hutcheon and Yarom 2000; Narayanan and Johnston 2008). The primary effect of g_H on the membrane
658 impedance (Fig. 6B,C), is actually the same as in other neurons, a reduction of lowpass filtering and
659 impedance delay. Whether g_H narrows the membrane bandpass properties or broadens them, as it does
660 here and in CA3 interneurons (Anderson et al. 2011), depends on the relative balance of its effects and
661 those of other membrane properties.

662 In addition to showing low frequency variation and delays between I_m and V_m , the impedance
663 of the LGMD also showed consistency across holding potentials. As an object approaches, increasing
664 excitation causes dendritic depolarization of >20 mV, so changes in dendritic integration properties
665 with membrane potential would influence the detection of impending collisions. Neither the amplitude
666 nor the phase of the membrane impedance changed much from -70 to -55 mV (Fig. 3 and 4). This
667 consistency can also be largely explained by g_H and g_M. At hyperpolarized potentials g_H increases,
668 dominating the membrane conductance, while conversely g_M increases with depolarization. At the
669 LGMD's resting membrane potential (-65 mV), both channels have large conductances and shallow
670 activation kinetics (Dewell and Gabbiani 2018a, 2018b). If the activation ranges of g_H and g_M had less

overlap, the impedance profile would be less consistent across membrane potentials and the channels would be more likely to create separate hyperpolarized and depolarized resonances as seen in pyramidal cells (Hu et al. 2002, 2009).

Synaptic integration is influenced by the input timing as well as its gain. We found that the LGMD exhibited shorter delays between I_m and V_m than could be explained by a circuit model (Fig. 5H). These delays were reduced by both g_H and g_M (Fig. 6I). On average, blockade of g_M produced a larger reduction than g_H, except at frequencies near the peak membrane power during looming stimuli (~1.3 Hz; Fig. 2F). The influence of g_H at low frequencies is consistent with its effect on synaptic pattern discrimination during looming (Dewell and Gabbiani 2018a), while having only a small effect in model simulations with brief periods of excitatory inputs (Fig. 7A). In contrast, the ability to discriminate the timing of these simulated synaptic inputs was greatly reduced by removal of g_M from the LGMD model (Fig. 7), a feature that would be difficult to test experimentally because the g_M blocker XE991 also has presynaptic effects (Dewell and Gabbiani 2018b). Previously, simulations of these same brief periods of excitation using a model of a CA1 pyramidal neuron found g_H to dramatically increase sensitivity to input timing (Migliore et al. 2004). In those CA1 simulations the g_H time constant was ~40-fold faster than in our LGMD model, but it was very similar to the LGMD's g_M time constant. This further supports the idea that these effects are mainly due to the change in membrane impedance, rather than channel type.

Although g_H and g_M decreased I_m-V_m delays, the delays remained lower after their blockade than those of an equivalent circuit model. Testing a morphologically realistic, passive LGMD model revealed that the neuron's shape influenced the membrane's input impedance as much as the active conductances (Fig. 8A, B). The branching morphology introduces new electrical paths whose axial resistivity does not decrease with frequency. This led to increased input gain and reduced input delays. Previous modeling of pyramidal and Purkinje neurons have also found that dendritic branches reduced lowpass filtering (Dhupia et al. 2015; Ostojic et al. 2015). This led us to wonder how the influence of

696 LGMD's morphology on impedance compared to other cell morphologies, and whether the increase in
697 input impedance caused by an extended neuronal morphology was counteracted by decreased signal
698 propagation. We tested this with transfer impedance simulations of five neuronal morphologies.

699 Transfer impedance is defined between two locations. While it is technically infeasible to
700 simultaneously record intracellularly from many places within a neuron, in a model it is no more
701 difficult to measure transfer between one hundred locations than between two. The reason we chose to
702 measure the all-to-all transfer rather than just transfer from individual dendrites to the site of spike
703 initiation is simple. In neurons, *in vivo* synaptic currents impinge throughout the dendrites and do not
704 propagate in isolation, but continuously integrate with new inputs. As far as we know, this is the first
705 examination of the sum transfer of a dendritic arbor in this fashion. It revealed that in the LGMD, as
706 well as other cells, the net effect of morphology is an increase in all-to-all impedance gain and a
707 decrease in high frequency delay between I_m and V_m. Additionally, we found that the net increase in
708 gain is bandpass between 30 and 100 Hz (Fig. 8H). Although their magnitudes were consistent, the
709 frequency range of these changes depended on the simulated membrane time constant; for simulations
710 with a slower membrane the bandpass gain increase shifted to lower frequencies (data not shown). This
711 furthers previous findings on the effects of dendritic morphology on a neuron's integration capabilities
712 (Dhupia et al. 2015; Mainen and Sejnowski 1996; Moore et al. 1988).

713 Ultimately the integration properties of a neuron are dictated by the pattern of its inputs and its
714 computational role. For hippocampal pyramidal neurons that receive theta rhythmic inputs, a strong
715 theta (4-10 Hz) resonance and synchrony could be advantageous (Hu et al. 2009; Hutcheon and Yarom
716 2000; Vaidya and Johnston 2013). Similarly, it might be a computational benefit for cortical neurons to
717 exhibit large impedance changes with membrane potential to enhance differences between up and
718 down network states (Gutfreund et al. 1995b; Hasselmo 2005; Heys et al. 2010; Wang 2010). For
719 auditory neurons, specialized in detecting high frequency sound waves, a very fast membrane time
720 constant and high frequency inductance lead to broadband membranes with resonance at frequencies

721 up to 400 Hz (Mikiel-Hunter et al. 2016; Remme et al. 2014). The LGMD detects approaching objects
722 and discriminates their specific input statistics from a wide range of other input patterns through their
723 integration over a wide range of membrane potentials. This involves discriminating synaptic input
724 patterns on the order of milliseconds to tens of milliseconds (Jones and Gabbiani 2010) as well as over
725 several seconds (Dewell and Gabbiani 2018a). Thus, achieving broadband membrane impedance with
726 minimal delay across input frequencies and membrane potentials by a balance of active membrane
727 conductances and an extended morphology is exactly what is needed to fine tune escape behaviors.

728 **References:**

729 **Anderson WD**, **Galván EJ**, **Mauna JC**, **Thiels E**, **Barrionuevo G**. Properties and functional
730 implications of I_h in hippocampal area CA3 interneurons. *Pflügers Archiv - European Journal of*
731 *Physiology* 462: 895–912, 2011.

732 **Barrow AJ**, **Wu SM**. Low-Conductance HCN1 Ion Channels Augment the Frequency Response of
733 Rod and Cone Photoreceptors. *Journal of Neuroscience* 29: 5841–5853, 2009.

734 **Cole KS**. Rectification and inductance in the squid giant axon. *The Journal of General Physiology* 25:
735 29–51, 1941.

736 **Cuntz H**, **Borst A**, **Segev I**. Optimization principles of dendritic structure. *Theoretical Biology and*
737 *Medical Modelling* 4: 21, 2007.

738 **Das A**, **Rathour RK**, **Narayanan R**. Strings on a Violin: Location Dependence of Frequency Tuning
739 in Active Dendrites. *Frontiers in Cellular Neuroscience* 11, 2017.

740 **Delmas P**, **Brown DA**. Pathways modulating neural KCNQ/M (Kv7) potassium channels. *Nature*
741 *Reviews Neuroscience* 6: 850–862, 2005.

742 **Dewell RB**, **Gabbiani F**. Biophysics of object segmentation in a collision-detecting neuron. *eLife* 7:
743 e34238, 2018a.

744 **Dewell RB**, **Gabbiani F**. M current regulates firing mode and spike reliability in a collision detecting
745 neuron. *J Neurophysiol* 120: 1753–1764, 2018b.

746 **Dhupia N**, **Rathour RK**, **Narayanan R**. Dendritic atrophy constricts functional maps in resonance
747 and impedance properties of hippocampal model neurons. *Frontiers in Cellular Neuroscience* 8, 2015.

748 **Eyal G**, **Verhoog MB**, **Testa-Silva G**, **Deitcher Y**, **Lodder JC**, **Benavides-Piccione R**, **Morales J**,
749 **DeFelipe J**, **de Kock CP**, **Mansvelder HD**, **Segev I**. Unique membrane properties and enhanced
750 signal processing in human neocortical neurons. *eLife* 5, 2016.

751 **Fotowat H**, **Harrison RR**, **Gabbiani F**. Multiplexing of Motor Information in the Discharge of a
752 Collision Detecting Neuron during Escape Behaviors. *Neuron* 69: 147–158, 2011.

Gabbiani F, **Krapp HG**. Spike-Frequency Adaptation and Intrinsic Properties of an Identified, Looming-Sensitive Neuron. *Journal of Neurophysiology* 96: 2951–2962, 2006a.

Gabbiani F, **Krapp HG**, **Koch C**, **Laurent G**. Multiplicative computation in a visual neuron sensitive to looming. *Nature* 420: 320–324, 2002.

Gabbiani F, **Mo C**, **Laurent G**. Invariance of Angular Threshold Computation in a Wide-Field Looming-Sensitive Neuron. *J Neurosci* 21: 314, 2001.

Gastrein P, **Campanac émilie**, **Gasselin C**, **Cudmore RH**, **Bialowas A**, **Carlier E**, **Fronzaroli-Molinieres L**, **Ankri N**, **Debanne D**. The role of hyperpolarization-activated cationic current in spike-time precision and intrinsic resonance in cortical neurons *in vitro*: I_h and neuronal timing. *The Journal of Physiology* 589: 3753–3773, 2011.

Gray JR, **Robertson RM**, **Lee JK**. Activity of descending contralateral movement detector neurons and collision avoidance behaviour in response to head-on visual stimuli in locusts. *Journal of Comparative Physiology A: Sensory, Neural, and Behavioral Physiology* 187: 115–129, 2001.

Gutfreund Y, **yarom Y**, **Segev I**. Subthreshold oscillations and resonant frequency in guinea-pig cortical neurons: physiology and modelling. *The Journal of Physiology* 483: 621–640, 1995a.

Hasselmo ME. What is the function of hippocampal theta rhythm?—Linking behavioral data to phasic properties of field potential and unit recording data. *Hippocampus* 15: 936–949, 2005.

Häusser M, **Mel B**. Dendrites: bug or feature? *Current Opinion in Neurobiology* 13: 372–383, 2003.

Heys JG, **Giocomo LM**, **Hasselmo ME**. Cholinergic Modulation of the Resonance Properties of Stellate Cells in Layer II of Medial Entorhinal Cortex. *Journal of Neurophysiology* 104: 258–270, 2010.

Holmes WR, **Segev I**, **Rall W**. Interpretation of time constant and electrotonic length estimates in multicylinder or branched neuronal structures. *Journal of Neurophysiology* 68: 1401–1420, 1992.

Hönigsperger C, **Marosi M**, **Murphy R**, **Storm JF**. Dorsoventral differences in Kv7/M-current and its impact on resonance, temporal summation and excitability in rat hippocampal pyramidal cells: Kv7/M-channel differences in dorsal and ventral CA1 pyramidal cells. *The Journal of Physiology* 593: 1551–1580, 2015.

Horowitz P, **Hill W**. The Art of Electronics. *The Art of Electronics, by Paul Horowitz, Winfield Hill, Cambridge, UK: Cambridge University Press, 2015* , 2015.

Hu H, **Vervaeke K**, **Graham LJ**, **Storm JF**. Complementary Theta Resonance Filtering by Two Spatially Segregated Mechanisms in CA1 Hippocampal Pyramidal Neurons. *Journal of Neuroscience* 29: 14472–14483, 2009.

Hu H, **Vervaeke K**, **Storm JF**. Two forms of electrical resonance at theta frequencies, generated by M-current, h-current and persistent Na^+ current in rat hippocampal pyramidal cells. *The Journal of Physiology* 545: 783–805, 2002.

Hutcheon B, **Miura RM**, **Puil E**. Subthreshold membrane resonance in neocortical neurons. *Journal of Neurophysiology* 76: 683–697, 1996.

Hutcheon B, **Yarom Y**. Resonance, oscillation and the intrinsic frequency preferences of neurons. *Trends in Neurosciences* 23: 216–222, 2000.

Jaffe DB, **Carnevale NT**. Passive Normalization of Synaptic Integration Influenced by Dendritic Architecture. *Journal of Neurophysiology* 82: 3268–3285, 1999.

Jones PW, **Gabbiani F**. Synchronized Neural Input Shapes Stimulus Selectivity in a Collision-Detecting Neuron. *Current Biology* 20: 2052–2057, 2010.

Jones PW, **Gabbiani F**. Impact of neural noise on a sensory-motor pathway signaling impending collision. *Journal of Neurophysiology* 107: 1067–1079, 2012.

Koch C. Cable theory in neurons with active, linearized membranes. *Biological Cybernetics* 50: 15–33, 1984a.

London M, **Hausser M**. Dendritic Computation. *Annual Reviews of Neuroscience* 28: 503–32, 2005.

Mainen ZF, **Sejnowski TJ**. Influence of dendritic structure on firing pattern in model neocortical neurons. *Nature* 382: 363–366, 1996.

Mauro A. Anomalous Impedance, A Phenomenological Property of Time-Variant Resistance. *Biophysical Journal* 1: 353–372, 1961.

Mauro A, **Conti F**, **Dodge F**, **Schor R**. Subthreshold Behavior and Phenomenological Impedance of the Squid Giant Axon. *The Journal of General Physiology* 55: 497–523, 1970.

McGinley MJ, **Liberman MC**, **Bal R**, **Oertel D**. Generating Synchrony from the Asynchronous: Compensation for Cochlear Traveling Wave Delays by the Dendrites of Individual Brainstem Neurons. *Journal of Neuroscience* 32: 9301–9311, 2012.

McMillan GA, **Gray JR**. Burst Firing in a Motion-Sensitive Neural Pathway Correlates with Expansion Properties of Looming Objects that Evoke Avoidance Behaviors. *Frontiers in Integrative Neuroscience* 9, 2015.

Migliore M, **Messineo L**, **Ferrante M**. Dendritic I_h Selectively Blocks Temporal Summation of Unsynchronized Distal Inputs in CA1 Pyramidal Neurons. *Journal of Computational Neuroscience* 16: 5–13, 2004.

Mikiel-Hunter J, **Kotak V**, **Rinzel J**. High-Frequency Resonance in the Gerbil Medial Superior Olive. *PLOS Computational Biology* 12: e1005166, 2016.

Miyasho T, **Takagi H**, **Suzuki H**, **Watanabe S**, **Inoue M**, **Kudo Y**, **Miyakawa H**. Low-threshold potassium channels and a low-threshold calcium channel regulate Ca^{2+} spike firing in the dendrites of cerebellar Purkinje neurons: a modeling study. *Brain Research* 891: 106–115, 2001.

Moore LE, **Yoshii K**, **Christensen BN**. Transfer impedances between different regions of branched excitable cells. *Journal of Neurophysiology* 59: 689–705, 1988.

Narayanan R, **Johnston D**. The h Channel Mediates Location Dependence and Plasticity of Intrinsic Phase Response in Rat Hippocampal Neurons. *Journal of Neuroscience* 28: 5846–5860, 2008.

825 **O'Shea M**, **Williams JLD**. The anatomy and output connection of a locust visual interneurone; the
826 lobular giant movement detector (LGMD) neurone. *Journal of Comparative Physiology* 91: 257–266,
827 1974.

828 **Ostojic S**, **Szapiro G**, **Schwartz E**, **Barbour B**, **Brunel N**, **Hakim V**. Neuronal Morphology
829 Generates High-Frequency Firing Resonance. *Journal of Neuroscience* 35: 7056–7068, 2015.

830 **Peron S**, **Gabbiani F**. Spike frequency adaptation mediates looming stimulus selectivity in a collision-
831 detecting neuron. *Nature Neuroscience* 12: 318–326, 2009.

832 **Peron SP**, **Krapp HG**, **Gabbiani F**. Influence of Electrotonic Structure and Synaptic Mapping on the
833 Receptive Field Properties of a Collision-Detecting Neuron. *Journal of Neurophysiology* 97: 159–177,
834 2007a.

835 **Rall W**. Theoretical significance of dendritic trees for neuronal input-output relations. *Neural theory*
836 *and modeling* 73–97, 1964.

837 **Remme MWH**, **Donato R**, **Mikiel-Hunter J**, **Ballestero JA**, **Foster S**, **Rinzel J**, **McAlpine D**.
838 Subthreshold resonance properties contribute to the efficient coding of auditory spatial cues.
839 *Proceedings of the National Academy of Sciences* 111: E2339–E2348, 2014.

840 **Rind FC**, **Simmons PJ**. Orthopteran DCMD neuron: a reevaluation of responses to moving objects. I.
841 Selective responses to approaching objects. *Journal of Neurophysiology* 68: 1654–1666, 1992.

842 **Rind FC**, **Wernitznig S**, **Pölt P**, **Zankel A**, **Gütl D**, **Sztarker J**, **Leitinger G**. Two identified looming
843 detectors in the locust: ubiquitous lateral connections among their inputs contribute to selective
844 responses to looming objects. *Scientific Reports* 6, 2016.

845 **Schlotterer GR**. Response of the locust descending movement detector neuron to rapidly approaching
846 and withdrawing visual stimuli. *Canadian Journal of Zoology* 55: 1372–1376, 1977.

847 **Sekulić V**, **Chen T-C**, **Lawrence JJ**, **Skinner FK**. Dendritic distributions of Ih channels in
848 experimentally-derived multi-compartment models of oriens-lacunosum/moleculare (O-LM)
849 hippocampal interneurons. *Frontiers in Synaptic Neuroscience* 7, 2015.

850 **Ulrich D**. Dendritic Resonance in Rat Neocortical Pyramidal Cells. *Journal of Neurophysiology* 87:
851 2753–2759, 2002.

852 **Vaidya SP**, **Johnston D**. Temporal synchrony and gamma-to-theta power conversion in the dendrites
853 of CA1 pyramidal neurons. *Nature Neuroscience* 16: 1812–1820, 2013.

854 **Vetter P**, **Roth A**, **Häusser M**. Propagation of Action Potentials in Dendrites Depends on Dendritic
855 Morphology. *Journal of Neurophysiology* 85: 926–937, 2001.

856 **Wahl-Schott C**, **Biel M**. HCN channels: Structure, cellular regulation and physiological function.
857 *Cellular and Molecular Life Sciences* 66: 470–494, 2009.

858 **Wang X-J**. Neurophysiological and Computational Principles of Cortical Rhythms in Cognition.
859 *Physiological Reviews* 90: 1195–1268, 2010.

Zhu Y, **Gabbiani F**. Fine and distributed subcellular retinotopy of excitatory inputs to the dendritic tree of a collision-detecting neuron. *Journal of Neurophysiology* 115: 3101–3112, 2016.

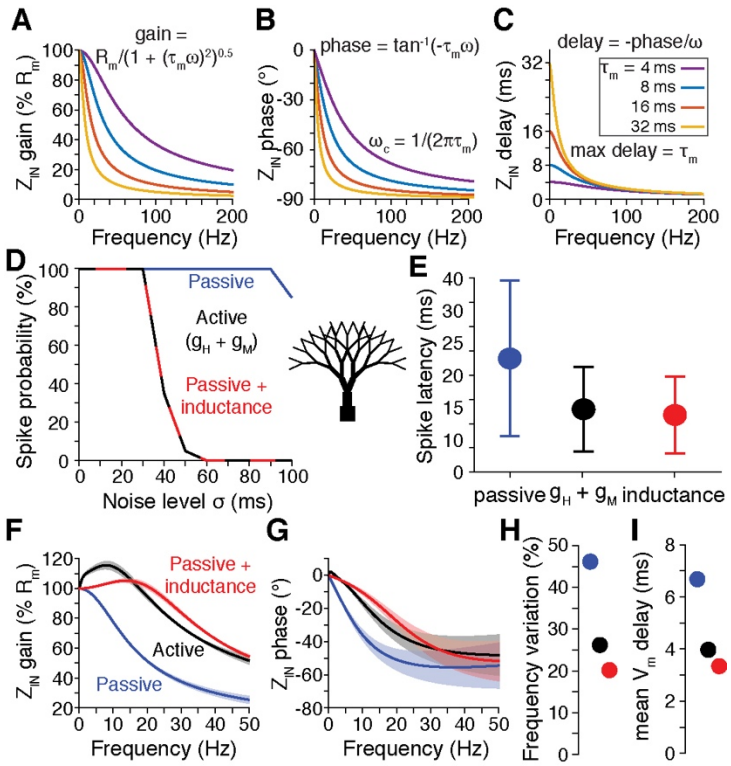

Figure 1. Membrane impedance shapes the ability of neurons to discriminate and transmit the timing of their inputs. A) The membrane impedance amplitude of a passive isopotential neuron (modeled as an RC circuit) decays with frequency, more rapidly so the slower the membrane time constant (τ_m). The impedance amplitude determines the gain between input currents and membrane potential. Formula: R_m – membrane resistance; ω – frequency (radian). B) The impedance phase, which determines the timing between input currents and membrane potential, also decreases with frequency in passive isopotential neurons. The corner frequency (ω_c) of the membrane impedance for such RC models is determined by the τ_m. C) Converting the phase into the time domain reveals that for low frequency signals the delay between membrane current and potential equals τ_m and that this delay depends on frequency. D) Simulations with a Rall branching neuron model (schematic at right) tested the ability to discriminate the synchrony of 100 synaptic inputs. If the model contained the active conductances g_H and g_M, spikes were generated by synchronous inputs but not if input synchrony was decreased by adding random noise to the synaptic activation times (black). Removal of the active conductances greatly decreased the ability to discriminate the timing of synaptic inputs (blue). If the voltage dependent conductances were replaced by a voltage independent inductance, the ability to

discriminate input timing was returned. E) The timing of spikes changed accordingly, such that for the models with inductances the spike time more faithfully conveyed the timing of its inputs. F,G) The voltage independent inductance produced similar changes to the impedance gain (F) and impedance timing (G) as did the voltage dependent conductances. H) The passive model had higher frequency variation indicating that it was more lowpass and less broadband. I) The mean absolute delay between I_m and V_m was higher for the passive model, causing the reduction in timing reliability for the model.

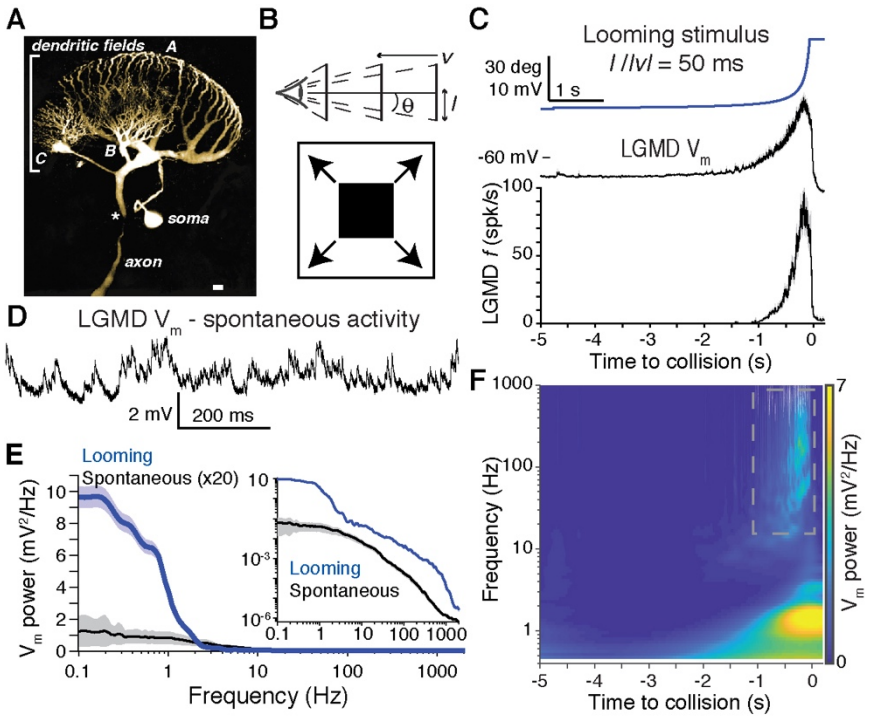

Dewell and Gabbiani, Fig. 2

Figure 2. Spontaneous and looming stimulus-evoked spectral power density of the LGMD's membrane potential. A) Micrograph of the LGMD, illustrating its dendritic fields (labeled A, B and C), the spike initiation zone (SIZ, marked with *) at the start of the axon, and the soma which lies outside of the neuron's electrical signal path (adapted from Gabbiani et al., 2002). Scale bar: 25 µm. B) A looming stimulus consists of a black square expanding symmetrically on the animal's retina (bottom). It simulates an object of half size l approaching on a collision course at constant velocity v (< 0), subtending an angular size $2\theta(t)$ at the retina (top). C) Looming stimuli produce an angular size that increases nonlinearly over time (top, blue line). Most of the response to looming stimuli occurs shortly before the projected time of collision as can be seen in the average membrane potential (V_m, middle) and firing rate (bottom, displayed as mean ± standard error of the mean, sem, for 59 looming stimuli; N = 16 animals). D) Example recording of dendritic membrane potential within the LGMD while the eye was exposed to uniform illumination (V_m low-pass filtered at 10 kHz and digitized at 40 kHz). E) Despite the high frequency of spontaneous inputs, the V_m power is concentrated at frequencies below 5 Hz (black, abscissa is on logarithmic scale). During looming stimuli, the signal power increased 125-fold but remained concentrated at low frequencies (blue). Inset shows the data on a double logarithmic scale. Solid lines and shaded regions are mean ± sem (N = 16 animals). F) Using wavelet analysis to measure the membrane potential power density in both the frequency and time domains reveals that during spiking there is increased high frequency power (dashed square), but the peak power remains at

904 frequencies <10 Hz. Plot displays the average power density map of the same 59 looming responses
905 shown in C and E.
906

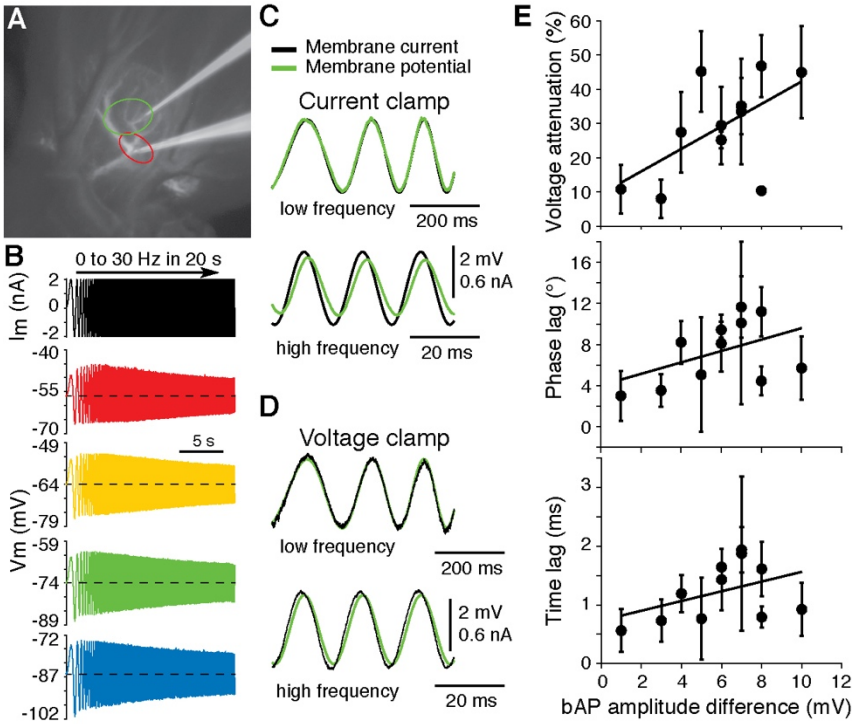

907 Dewell and Gabbiani, Fig. 3

908 **Figure 3.** Characterization of LGMD's membrane impedance profile with *in vivo* dendritic recordings.
909 A) Either single or dual recordings were made from dendritic field A and the primary neurite
910 connecting field A to the SIZ. Image taken with a CCD camera during a dual recording after staining
911 the LGMD with Alexa 594. The internal solution of both electrodes contained Alexa 594 for
912 visualization. Red and green ellipses encompass the region sampled by the proximal and distal
913 electrode, respectively, across 12 recording pairs (8 animals). B) To measure membrane impedance,
914 chirp currents (sine waveforms of increasing frequency) were injected at different steady-state
915 membrane potentials (V_{ss}). At top is an example of a linearly increasing chirp current followed by four
916 recordings of the membrane potential in response to this chirp current superposed on different holding
917 currents (I_{hold}). The values of I_{hold} and V_{ss} (dashed lines) were 2, 0, -2, -4 nA and -56, -64, -74, -86 mV,
918 respectively (from top to bottom). C) Examples traces of low and high frequency sections of the
919 measured membrane current and potential. At low frequencies the current and potential are
920 synchronous (~0° impedance phase) but at high frequencies the potential trails the current (negative
921 impedance phase). Note that at high frequencies the membrane potential is reduced relative to the
922 current indicating a reduction in impedance amplitude. D) Impedance measurements were similar

923 when measured in voltage clamp. E) Signals attenuated more and had longer lags as the electrotonic
924 distance increased between recording electrodes (estimated by the difference in amplitudes of the
925 backpropagating action potential, bAP). Each point and error bar report the mean value and sd (across
926 different V_{ss} values) for a recording pair (N = 11 recording pairs from 8 animals). Mean bAP
927 amplitudes were 32 and 26 mV for the proximal and distal electrode; the dendritic path distance
928 between recordings ranged from 63 to 149 µm with a mean of 105 µm.
929

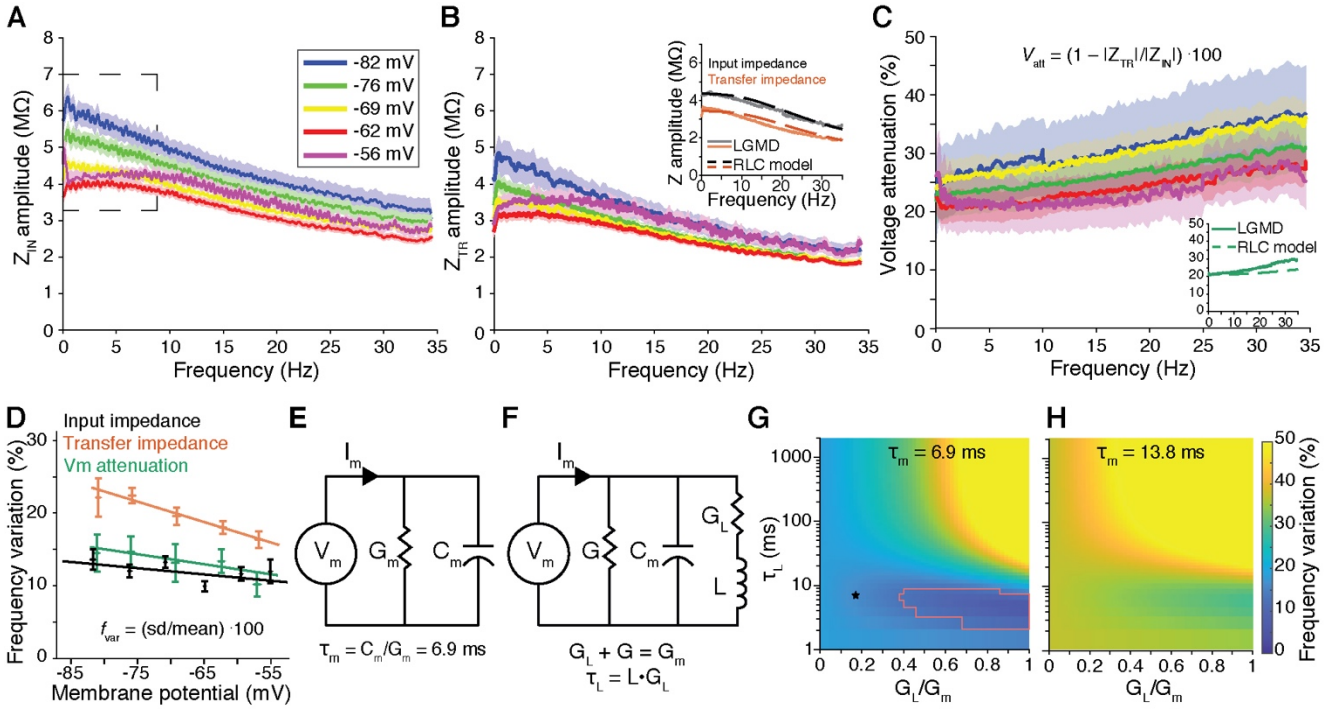

Dewell and Gabbiani, Fig. 4

Figure 4. The LGMD membrane impedance amplitude and voltage attenuation behave similarly across frequencies and membrane potentials. A) Input impedance (Z_{IN}) amplitude profiles measured at different steady-state membrane potentials (V_{ss}, see Fig. 3B) and displayed as mean ± sem (lines and shaded regions) reveal a high degree of overlap across membrane potentials. The lines only show clear separation for low frequencies (<10 Hz, dashed square) at membrane potentials >10 mV below V_{rest} (-65 mV). N = 76 recordings from 56 animals. B) The transfer impedance (Z_{TR}) amplitude between different dendritic sites also varied little across membrane potentials. The inset shows the average input and transfer impedance amplitudes (solid lines) overlaid with those of an RLC circuit model as depicted in panel F (dashed lines). N = 13 recording pairs from 10 animals. C) Voltage attenuation (V_{att}) is more variable between recordings than impedance amplitude (note the larger sem regions in C when compared to A or B) with ~20–35% reduction in voltage between dendritic locations. The inset compares attenuation with that of the best-fit RLC model of panel F. Same data set as in B. D) The frequency variation (f_{var}) of the input and transfer impedance amplitude as well as that of voltage attenuation decreased slightly with membrane depolarization. The frequency variation shows the consistency across frequencies, with a value of 0 indicating an ideal resistor. E,F) RC and RLC circuits, respectively, were chained to obtain equivalent cylinder models for comparison with the data. For both circuit models G_m = 116 μS/cm^2 and C_m = 0.8 μF/cm^2. See methods for details on impedance calculations. G) Heatmap illustrating the effect of the RLC circuit inductor parameters on the

frequency variation of its input impedance. The left edge ($G_L = 0$) corresponds to the RC circuit depicted in E. Slower inductor time constants (τ_L) increased frequency variation. Increasing the ratio G_L/G_m increased frequency variability for slow inductors and decreased it for fast inductors. The red line delimits the parameter region that had a frequency variation as low as the LGMD data. The star indicates the parameter values used for the insets in panels B and C which best matched the shape of the LGMD impedance amplitude profiles. H) Heatmap of an RLC circuit with τ_m twice that of the LGMD. For this slower circuit model, no inductor parameter yielded an impedance as consistent across frequencies as the LGMD data. In G and H plotted values are for input impedance; transfer impedance maps look similar but with frequency variations of ~1.06 times those in the input impedance maps for all parameters.

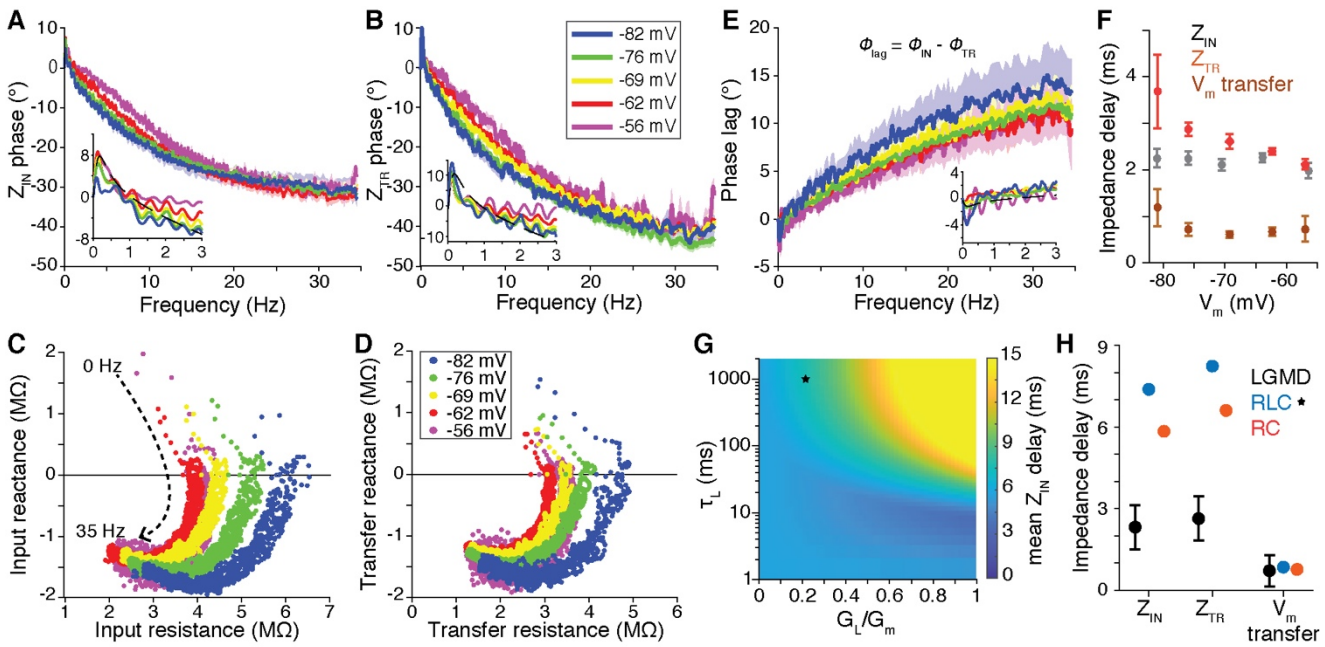

Dewell and Gabbiani, Fig. 5

Figure 5. LGMD membrane synchrony and consistency across membrane potentials. A) Z_{IN} phase profiles (mean ± sem) are inductive (exhibit positive phase) only at frequencies < 1 Hz (inset), show high overlap across membrane potentials, and level off around -30°. N = 76 recordings from 56 animals. B) Z_{TR} phases similarly exhibit induction at frequencies < 1 Hz (inset) and overlap across membrane potentials. N = 13 recording pairs from 10 animals. C, D) Impedance locus plots show the real (resistance) and imaginary (reactance) components of the impedance, pooled across frequencies (dotted arrow). The membrane inductance at low frequencies is evidenced by the points with positive reactance. At hyperpolarized potentials, resistance increased but otherwise the LGMD maintained a consistent profile across membrane potentials. E) Phase lag of membrane potential at the 'recording-only' location relative to that at the 'recording and current injection' location. At frequencies <1 Hz there was a phase advance with the more distant location preceding the input location (inset). The phase lag increased steadily with frequency. F) Impedance delay was measured as the mean absolute time lag between pairs of simultaneously recorded variables. Z_{IN} delay corresponds to the lag between the input current and local membrane potential. Z_{TR} delay was calculated from the lag between the input current and membrane potential at the secondary recording location and V_m transfer delay from the lag between the membrane potentials at the two recording locations. Z_{TR} delay decreased with membrane depolarization. G) RLC circuit Z_{IN} delay as a function of its inductor parameters. Z_{TR} delay was ~1.1 times higher than Z_{IN} values shown. The LGMD low frequency inductive phase could only be reproduced by a slow inductor. Dashed black lines in insets of A, B and E produced by parameters

marked by black star in G. H) The LGMD exhibited lower delay between membrane current and voltage (phase nearer 0°) than an RC circuit model ($G_L = 0$) or the RLC circuit model marked by the black star in G. No RLC circuit with comparable time constant produced as small a mean Z_{IN} or Z_{TR} delay as the LGMD.

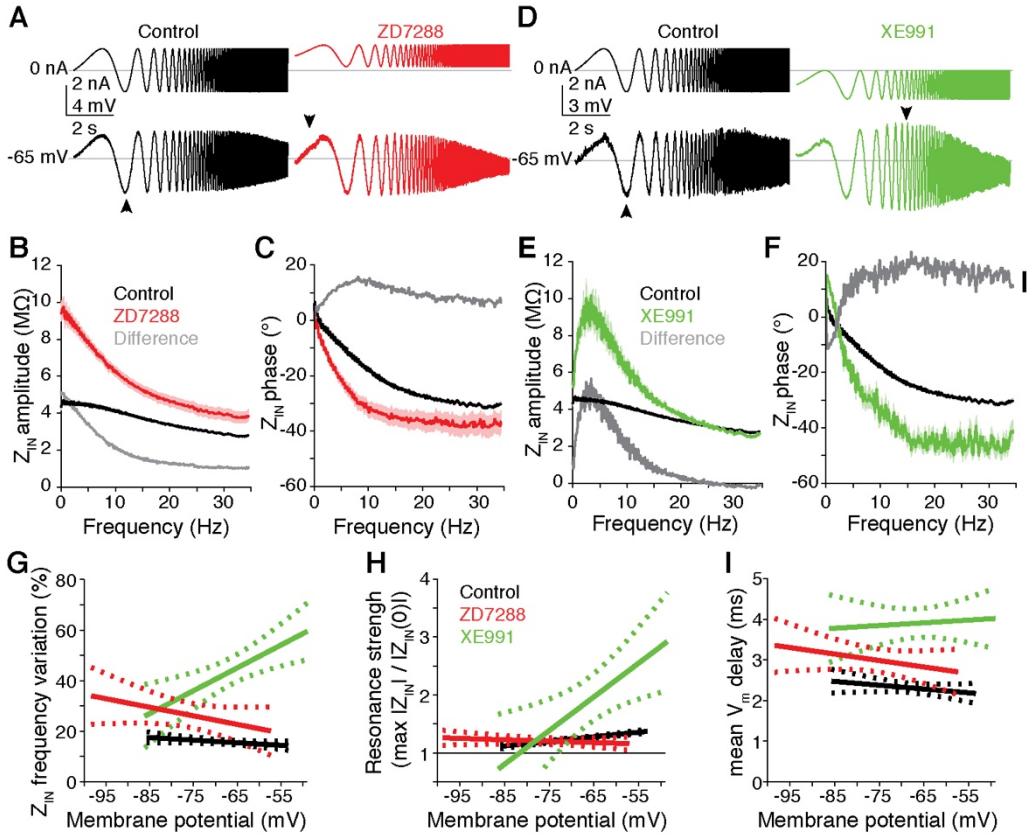

Dewell and Gabbiani, Fig. 6

Figure 6. Blockade of either HCN or M channels increased impedance frequency variation and delay between I_m and V_m. A) Example chirp currents (top) and membrane potential responses (bottom) before (left, black) and after (right, red) ZD7288 application. After drug application the chirp amplitude was decreased and I_{hold} was increased to produce a similar V_{ss} and similar changes in membrane potential. B) After blocking HCN channels with ZD7288, input impedance increased 2-fold at low frequencies. Population average impedance (across animals and V_{ss}) is shown as mean ± sem (solid line and shaded region). The grey line is the difference between the averages. C) Impedance phase decreased at all frequencies after HCN blockade, reducing membrane current-voltage synchrony. D) Example chirp currents (top) and response (bottom) before (left) and after (right) XE991 application. After drug application the chirp amplitude and I_{hold} were decreased to produce a similar V_{ss} and similar changes in membrane potential. E) After blocking M channels with XE991 a large increase in low frequency input impedance was also seen with peak at ~4 Hz. F) After M channel block impedance phase increased at low frequencies (<2 Hz) but decreased at higher frequencies. G) The increased low frequency impedance after blockade of HCN or M channels produced higher Z_{IN} frequency variations across steady-state membrane potentials. Z_{IN} frequency variation is displayed as linear fit (solid lines) and 95% confidence intervals (dotted lines). M channel blockade increased

1000 variation mainly at depolarized potentials while HCN blockade had a greater effect at hyperpolarized
1001 potentials. H) The resonance strength, calculated as the maximum impedance amplitude divided by
1002 steady-state impedance amplitude ($|Z_{IN}(0)|$), was <1.2 for all membrane potentials under control
1003 conditions and after HCN block. After I_M block, however, a larger resonance was observed at
1004 depolarized membrane potentials. I) The mean absolute time lag between the input current and local
1005 membrane potential, increased by ~1 ms after HCN block (red) and ~2 ms after M channel block
1006 (green). Control data (black) is the same as shown in Fig. 5F. Control data from 53 recordings at 181
1007 V_{ss} from 44 animals; ZD7288 data includes 9 recordings at 36 V_{ss} from 6 animals; XE991 data
1008 includes 6 recordings at 14 V_{ss} from 6 animals.
1009

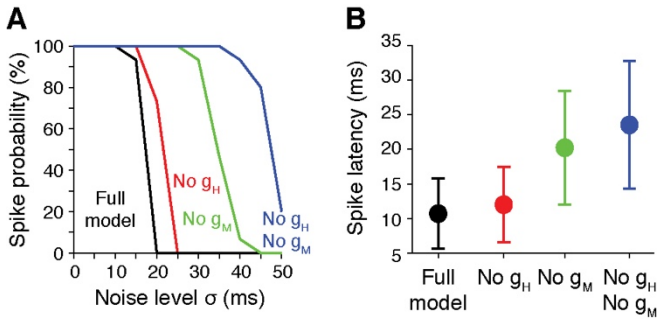

Dewell and Gabbiani, Fig. 7

Figure 7. LGMD model simulations show g_H and g_M increase sensitivity to synaptic input timing and reduce spike latency. A) In the full LGMD model (black), synchronous inputs reliably generated spikes, but for inputs with less reliable input timing ($\sigma > 15$ ms) no spikes were produced. Removal of g_H (red) slightly decreased the input timing selectivity, and removal of g_M (green) or both conductances (blue) produced larger reductions in the timing discrimination. In each condition the leak reversal potential was adjusted to maintain a constant resting membrane potential. B) The timing of the spikes generated were also less reliable. The full LGMD model generated spikes with the shortest latency after the inputs began. After g_M blockade spikes occurred later and with less reliable timing.

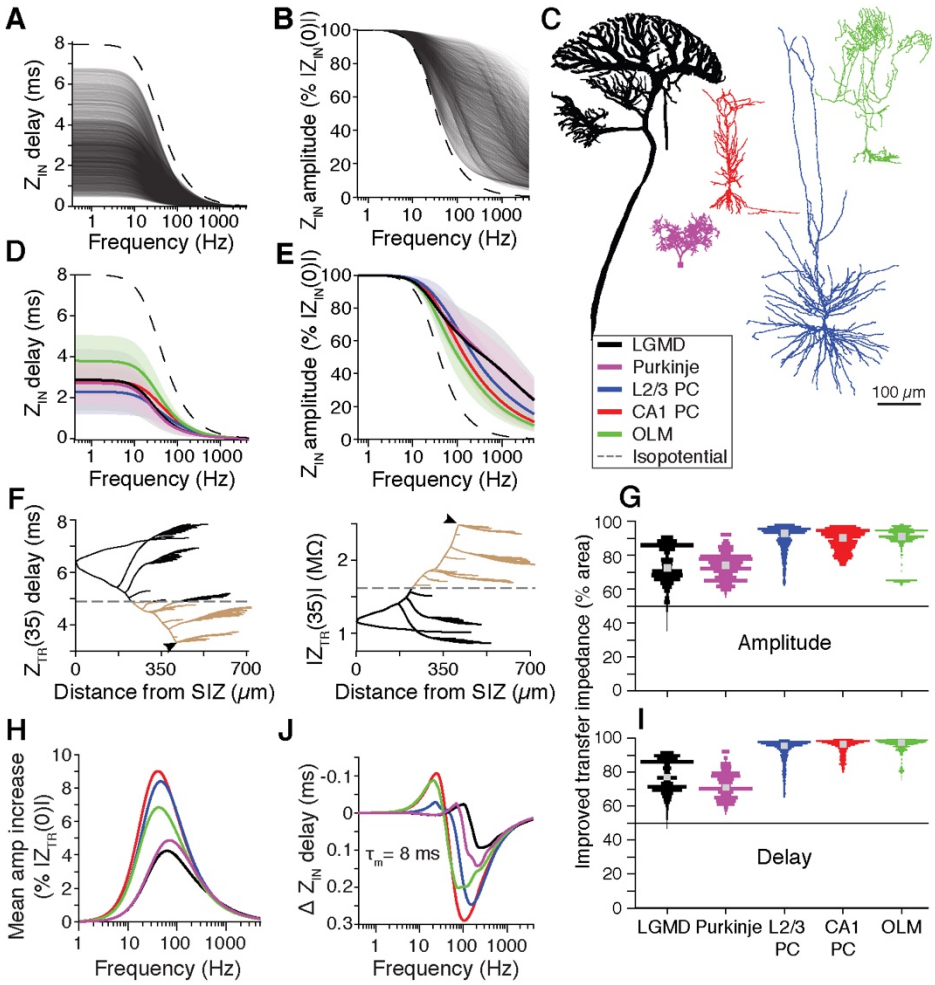

Figure 8. Simulations of passive neurons reveal the influence of morphology on impedance characteristics. A) Every section of the LGMD model (thin black lines) had shorter input impedance delays than an isopotential model (dashed line). B) All sections of the LGMD model (thin black lines) exhibited a decrease in input impedance amplitude smaller than that of an isopotential model (dashed line). For each section the impedance amplitude is normalized to impedance at 0 Hz ($|Z_{IN}(0)|$). The difference between the input impedance amplitude and that of an isopotential model was maximal at ~200 Hz. C) The effect of neuronal morphology on impedance was tested in the LGMD (black) and 4 other cell morphologies of different size and shape: a cerebellar Purkinje cell (purple), a hippocampal CA1 pyramidal cell (red), a cortical layer 2/3 pyramidal cell (blue), and a CA1 oriens lacunosum-moleculare interneuron (OLM; green). D) All neuron models tested had large decreases in input delay compared to an isopotential equivalent model. Data is color coded as depictions in C and presented as mean ± sd (solid lines and shaded regions). E) All morphologies had more consistent input impedance amplitude relative to their isopotential equivalents, with lower frequency variation. Data presented as in D. F) Data from example dendritic segments of the LGMD model shows that at 35 Hz the transfer

1035 impedance delay (left) increased and the amplitude (right) decreased with distance from the site of
1036 current injection (arrowheads). Segments for which transfer impedance had higher amplitude or shorter
1037 delay than that of an isopotential equivalent neuron (dashed line) are brown. Data in G and I measured
1038 by summing the surface area of brown segments and dividing by the total surface area. G) For each
1039 neuron model segment, we summed the surface area of other model segments for which signal transfer
1040 was increased compared to an isopotential equivalent and divided by the neuron's total surface area.
1041 Bar widths indicate how many model segments had improved transfer (higher gain and lower delay)
1042 for each percentage range, and grey squares mark the average segment. All morphologies had
1043 increased transfer amplitudes compared to an isopotential equivalent model, with the LGMD and
1044 Purkinje morphologies having improved transfer for a smaller percentage of the neuron segments. H)
1045 For all models, an average all-to-all transfer impedance was measured as a function of frequency and
1046 compared to the impedance of an isopotential equivalent. The increase of each cell's mean transfer
1047 amplitude as a function of frequency from isopotential reveals a bandpass increase in average transfer
1048 gain. I) The percentage of membrane area with reduced transfer delay was similar for each morphology
1049 as that with an increase in transfer gain. Plotted as in G. K) The average all-to-all transfer delay from
1050 I_m to V_m for each model was similar with no difference at low frequencies, a slightly longer delay near
1051 the frequency of the cell's peak gain, and reduced delays at higher frequencies.